The Astrophysical Journal, 926:37 (16pp), 2022 February 10 https://doi.org/10.3847/1538-4357/ac2b9f
© 2022. The Author(s). Published by the American Astronomical Society.
OPEN ACCESS

Spectroscopic Confirmation of a Protocluster at $z = 3.37$ with a High Fraction of Quiescent Galaxies

Ian McConachie[1], Gillian Wilson[1], Ben Forrest[1], Z. Cemile Marsan[2], Adam Muzzin[2], M. C. Cooper[3], Marianna Annunziatella[4,5], Danilo Marchesini[4], Jeffrey C. C. Chan[1], Percy Gomez[6], Mohamed H. Abdullah[1,7], Paolo Saracco[8], and Julie Nantais[9]

[1] Department of Physics and Astronomy, University of California, Riverside, 900 University Avenue, Riverside, CA 92521, USA; ian.mcconachie@email.ucr.edu
[2] Department of Physics and Astronomy, York University, 4700, Keele Street, Toronto, ON, MJ3 1P3, Canada
[3] Center for Cosmology, Department of Physics and Astronomy, University of California, Irvine, 4129 Frederick Reines Hall, Irvine, CA 92697-4575, USA
[4] Department of Physics and Astronomy, Tufts University, 574 Boston Avenue Suites 304, Medford, MA 02155, USA
[5] Centro de Astrobiología (CSIC-INTA), Ctra de Torrejón a Ajalvir, km 4, E-28850 Torrejón de Ardoz, Madrid, Spain
[6] W.M. Keck Observatory, 65-1120 Mamalahoa Highway, Kamuela, HI 96743, USA
[7] Department of Astronomy, National Research Institute of Astronomy and Geophysics, Helwan, 11421, Egypt
[8] INAF—Osservatorio Astronomico di Brera, via Brera 28, I-20121 Milano, Italy
[9] Departanento de Ciencias Físicas, Universidad Andrés Bello, Fernández Concha 700, Las Condes, Santiago, Chile
Received 2021 January 25; revised 2021 August 27; accepted 2021 September 28; published 2022 February 9

Abstract

We report the discovery of MAGAZ3NE J095924+022537, a spectroscopically confirmed protocluster at $z = 3.3665^{+0.0009}_{-0.0012}$ around a spectroscopically confirmed *UVJ*-quiescent ultramassive galaxy (UMG; $M_\star = 2.34^{+0.23}_{-0.34} \times 10^{11}\,M_\odot$) in the COSMOS UltraVISTA field. We present a total of 38 protocluster members (14 spectroscopic and 24 photometric), including the UMG. Notably, and in marked contrast to protoclusters previously reported at this epoch that have been found to contain predominantly star-forming members, we measure an elevated fraction of quiescent galaxies relative to the coeval field ($73.3^{+26.7}_{-16.9}$% versus $11.6^{+7.1}_{-4.9}$% for galaxies with stellar mass $M_\star \geqslant 10^{11} M_\odot$). This high quenched fraction provides a striking and important counterexample to the seeming ubiquitousness of star-forming galaxies in protoclusters at $z > 2$ and suggests, rather, that protoclusters exist in a diversity of evolutionary states in the early universe. We discuss the possibility that we might be observing either "early mass quenching" or nonclassical "environmental quenching." We also present the discovery of MAGAZ3NE J100028+023349, a second spectroscopically confirmed protocluster, at a very similar redshift of $z = 3.3801^{+0.0213}_{-0.0281}$. We present a total of 20 protocluster members, 12 of which are photometric and eight spectroscopic including a poststarburst UMG ($M_\star = 2.95^{+0.21}_{-0.20} \times 10^{11}\,M_\odot$). Protoclusters MAGAZ3NE J0959 and MAGAZ3NE J1000 are separated by 18′ on the sky (35 comoving Mpc), in good agreement with predictions from simulations for the size of "Coma"-type cluster progenitors at this epoch. It is highly likely that the two UMGs are the progenitors of Brightest Cluster Galaxies seen in massive virialized clusters at lower redshift.

Unified Astronomy Thesaurus concepts: Galaxy clusters (584); High-redshift galaxy clusters (2007); High-redshift galaxies (734); Large-scale structure of the universe (902); Brightest cluster galaxies (181); Quenched galaxies (2016); Galaxy evolution (594); Star formation (1569); Galaxy environments (2029)

1. Introduction

In the local universe, massive clusters (total mass $\geqslant 10^{15}\,M_\odot$) extend over only a few Mpc (e.g., Abdullah et al. 2020). However, numerical simulations have shown that the progenitors of these present-day clusters are very much more extended (Angulo et al. 2012; Chiang et al. 2013; Muldrew et al. 2015; Overzier 2016). For example, using the Millennium Simulation (Springel et al. 2005), Muldrew et al. (2015) found that, at $3 < z < 4$, 90% of the stellar mass of a protocluster with total mass $M_{z=0} = 10^{15.4}\,h^{-1}M_\odot$ typically extends over 65 comoving Mpc, corresponding to 14.5 physical Mpc or 31.5′ on the sky. In order to comprehensively study massive protoclusters at high redshift, observations spanning tens of arcminutes on the sky are required.

Closely related to the question of how protoclusters form in the early universe is how galaxies evolve within them. It has long been established that in the local universe there exists a strong dependence of galaxy properties on the environment, i.e., denser environments result in higher fractions of early-type galaxies (Oemler 1974; Dressler 1980; Binggeli et al. 1987; Goto et al. 2003; Fasano et al. 2012, 2015) and enhanced quenched fractions (Gómez et al. 2003; Kauffmann et al. 2004; Peng et al. 2010; Wetzel et al. 2012; Wang et al. 2018; Roberts & Parker 2019; Li et al. 2020). This is because galaxies in dense environments have been subject to "extra" external processes (environmental quenching) such as ram pressure stripping (Gunn et al. 1972), galaxy–galaxy interactions (Farouki & Shapiro 1981), harassment (Moore et al. 1996), and strangulation (Larson et al. 1980). These processes are in addition to "regular" internal processes (mass quenching), such as active galactic nuclei (AGNs; Fabian 2012) and stellar feedback (Hopkins et al. 2014). One of the most interesting questions in galaxy evolution is at what epoch environmental quenching first begins to take effect.

The most robust indicator of the presence of environmental quenching is an increase in the fraction of quiescent galaxies relative to that measured in the coeval field. Higher quiescent fractions have been observed out to $z \sim 2$, both directly from

Content from this work may be used under the terms of the Creative Commons Attribution 4.0 license. Any further distribution of this work must maintain attribution to the author(s) and the title of the work, journal citation and DOI.

analysis of spectroscopically confirmed clusters and groups (Muzzin et al. 2012; Quadri et al. 2012; Newman et al. 2014; Balogh et al. 2016; Cooke et al. 2016; Nantais et al. 2016, 2017; Lee-Brown et al. 2017; Lemaux et al. 2019; Pintos-Castro et al. 2019; Strazzullo et al. 2019; Zavala et al. 2019; van der Burg et al. 2020), and indirectly from statistical analysis of photometric overdensities (Cooper et al. 2006, 2007, 2010; Quadri et al. 2012; Darvish et al. 2016; Jian et al. 2017, 2018; Kawinwanichakij et al. 2017). However, efforts to detect environmental quenching at higher redshift have been hampered for two reasons: first, the practical difficulty of identifying and spectroscopically confirming protoclusters in the early universe, and second, the observational cost of acquiring the deep multi-passband photometric observations required to make a measurement of the quenched fraction.

One technique that has been successfully employed to identify protocluster systems in the early universe is to search for "overdensities" of, for example, Hα emitters (HAEs), Lyα emitters (LAEs), or Lyman-break galaxies (LBGs; e.g., Steidel et al. 1998; Lemaux et al. 2009, 2014; Dey et al. 2016; Ouchi et al. 2018; Toshikawa et al. 2018; Harikane et al. 2019; Shi et al. 2019; Guaita et al. 2020; Koyama et al. 2020). Another approach has been to target "signposts"—e.g., high-redshift radio galaxies (HzRGs; Pentericci et al. 1997; Miley & De Breuck 2008; Hatch et al. 2011; Galametz et al. 2012), quasi-stellar objects (QSOs; Adams et al. 2015), or dusty star-forming galaxies (DSFGs; Ivison et al. 2001, pp. 135–141; Long et al. 2020). A third technique has been to search for overdensities of DSFGs detected in the far-IR or submillimeter, e.g., in the Herschel Space Telescope, Planck Space Telescope, or South Pole Telescope surveys (Clements et al. 2014; Planck Collaboration et al. 2015, 2016; Greenslade et al. 2018; Miller et al. 2018; Cheng et al. 2019). Examples of protoclusters that have been discovered to date are notable in that they appear to be filled with star-forming galaxies (Chapman et al. 2009; Dannerbauer et al. 2014; Casey et al. 2015; Hung et al. 2016; Forrest et al. 2017). Indeed, some authors have suggested that starburst galaxies may be ubiquitous in protocluster systems (Casey 2016).

Here, we report on the discovery of two new protocluster systems, MAGAZ3NE J095924+022537 and MAGAZ3NE J100028+023349, confirmed to be at a similar redshift and at a separation of ∼35 comoving Mpc. The two systems were discovered not from a dedicated protocluster search but rather during a spectroscopic survey of a sample of ultramassive galaxies (UMGs; stellar mass $M_\star > 10^{11.0}\,M_\odot$) and their environments at $3 < z < 4$. Characterization of the properties of the 16 UMGs spectroscopically confirmed to date from this survey, the "Massive Ancient Galaxies At z > 3 NEar-infrared" (MAGAZ3NE) survey, has previously been presented in Forrest et al. (2020a; see also Forrest et al. 2020b).

The paper is organized as follows. In Section 2, we present the target selection, spectroscopic observations, data reduction, and determination of spectroscopic redshifts. In Section 3, we determine spectroscopic and photometric members of the protocluster systems. In Section 4, we calculate rest-frame *UVJ* colors and quiescent fractions. We discuss our results in Section 5 and present our main conclusions in Section 6. We assume $\Omega_m = 0.3$, $\Omega_\lambda = 0.7$, $H_0 = 70$ km s^{-1} Mpc^{-1}, and a Chabrier initial mass function (IMF; Chabrier 2003) throughout. All magnitudes are on the AB system (Oke & Gunn 1983).

2. Target Selection and MOSFIRE Observations

2.1. The COSMOS UltraVISTA Field

The COSMOS/UltraVISTA field contains the deepest, highest-quality multi-passband optical, infrared, and Spitzer IRAC imaging available over degree scales. This includes multi-passband imaging taken as part of the COSMOS survey (Capak et al. 2007), CFHT-Deep Legacy Survey (Hildebrandt et al. 2009), Subaru Strategic Program (SSP; Aihara et al. 2018), and UltraVISTA (McCracken et al. 2012) "ultra-deep stripes," providing an exquisite set of photometric measurements in multiple bands that can be used to estimate photometric redshifts, stellar masses, and rest-frame *UVJ* colors through spectral energy distribution (SED) modeling. The field is also covered by GALEX, Chandra, XMM-Newton, Herschel, SCUBA, and VLA, as well as spectroscopic surveys such as zCOSMOS (Lilly et al. 2007) and LEGA-C (van der Wel et al. 2016).

The unique quality and diversity of observations in the COSMOS UltraVISTA field have facilitated the discovery of protoclusters using a variety of techniques. These include X-ray emission (Finoguenov et al. 2007; Wang et al. 2016), and overdensities in photometric redshift (e.g., Chiang et al. 2014; Cucciati et al. 2018), distant red galaxies, LAEs, HAEs (Geach et al. 2012), radio sources (Daddi et al. 2017), or 3D Lyα forest tomography (Lee et al. 2014). Notable spectroscopically confirmed protoclusters at $z > 2$ that have been discovered in the COSMOS UltraVISTA field include systems at $z = 2.095$ (Spitler et al. 2012; Yuan et al. 2014; Casey 2016; Hung et al. 2016; Tran et al. 2017; Zavala et al. 2019), $z = 2.16$ (Koyama et al. 2020), $z = 2.232$ (Darvish et al. 2020), $z = 2.44$ ("Colossus"; Lee et al. 2016, see also Chiang et al. 2015), $z = 2.446$ ("Hyperion"; Diener et al. 2013, 2015; Chiang et al. 2014; Cucciati et al. 2018), $z = 2.47$ (Casey et al. 2015; Casey 2016; Zavala et al. 2019; Champagne et al. 2021), $z = 2.506$ (CLJ1001; Wang et al. 2016; Daddi et al. 2017), $z = 2.895$ (Cucciati et al. 2014, 2018), $z \sim 4.57$ (PCl J1001 +0220; Lemaux et al. 2018), $z \sim 5.3$ (Capak et al. 2011), and $z = 5.667$ (Pavesi et al. 2018).

The work presented here (target selection, SED fits, and photometric analysis) utilizes the COSMOS UltraVISTA Data Release Three (DR3) catalog (A. Muzzin et al. 2022, in preparation; see also Marsan et al. 2022), which was constructed using the techniques described in Muzzin et al. (2013) for the Data Release 1 (DR1) catalog. The DR3 catalog contains 50 photometric passbands ranging from *u*-band to MIPS 24 μm, and reaches a total $K_s$band 90% completeness at $K_{s,\mathrm{tot}} = 24.5$ AB in the 0.84 deg^2 "ultra-deep stripes" area (see Figure 1). The DR3 catalog is ∼1.5 magnitudes deeper in the *YJHK* bands than DR1 and also contains the new IRAC SMUVS data (Ashby et al. 2018), which is ∼1.2 magnitudes deeper than the S-COSMOS DR1 data (Sanders et al. 2007).

Best-fit photometric redshifts and rest-frame colors for galaxies in the catalog were obtained using EAZY (Brammer et al. 2008) and quantities such as star formation rate, stellar mass, and ages were calculated using FAST (Kriek et al. 2009). The photometry was fit to a set of models with exponentially declining star formation histories (SFR $\propto e^{-t/\tau}$), with a time since the onset of star formation (t) and a timescale for the decline in the SFR (τ). We used the models of Bruzual & Charlot (2003) with solar metallicity, a Calzetti et al. (2000) dust law, and assumed a Chabrier (2003) IMF. The variables were fit on a grid with $\log(\tau/\mathrm{yr})$ allowed to range between 7.0 and 10.0, $\log(t/\mathrm{yr})$

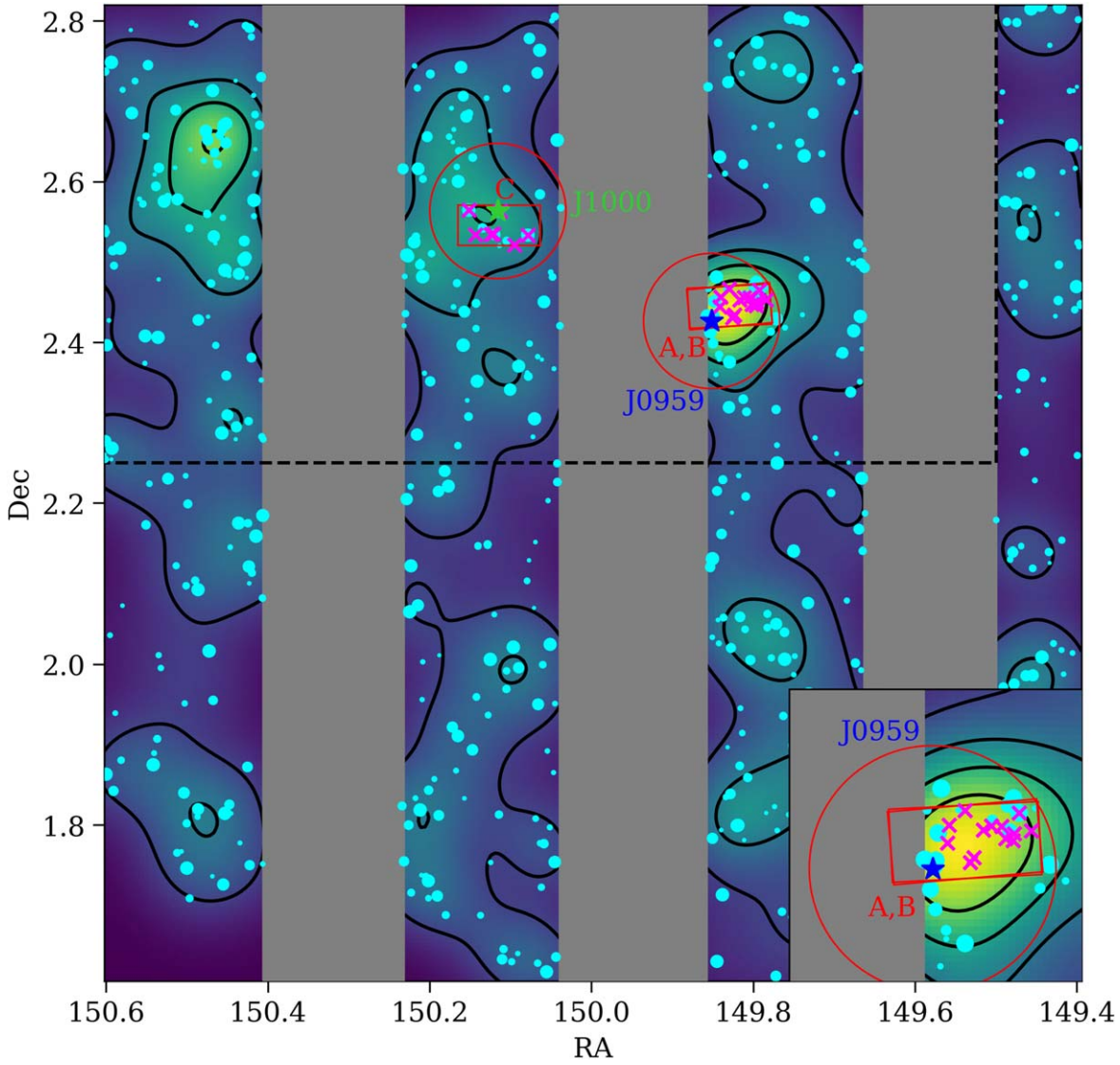

Figure 1. Density distribution of the 550 galaxies in the COSMOS UltraVISTA DR3 catalog (cyan circles) after photometric redshift, stellar mass, K_s-band magnitude, and probability cuts described in Section 3.2 have been applied. The size of each cyan circle is scaled by the integrated probability, P, of the galaxy lying in the redshift interval $z_{J0959} \pm 0.2$ (no galaxies appear in the gray vertical regions because of the "ultra-deep stripes" nature of the DR3 survey). The solid black contour lines indicate 80%, 60%, 40%, and 20% of the maximum density (yellow) and were calculated using a Gaussian kernel density estimator as described in Section 3.2. The two UMGs, UMG ID "COS-DR3-179370" (in protocluster MAGAZ3NE J095924+022537) and UMG ID "COS-DR3-160748" (in protocluster MAGAZ3NE J100028+023349), are shown by blue and green stars, respectively (see also Forrest et al. 2020b). They lie at a similar redshift and are separated by $\sim 18'$ on the sky. Spectroscopically confirmed protocluster members are shown by magenta crosses and the positions of the three MOSFIRE masks are indicated by red rectangles. The inset at the lower right is a zoom-in on the position of UMG 179370, showing the location of masks A and B (which had very similar centers and position angles and are, therefore, somewhat difficult to differentiate). Each of the two red circles has a radius of 10 comoving Mpc which is approximately equal to the Lagrangian radius. We define the members of protocluster MAGAZ3NE J0959 to be the 38 galaxies (14 magenta spectroscopic and 24 cyan photometric) that lie within the red circle centered on UMG 179370, and the members of protocluster MAGAZ3NE J1000 to be the 20 galaxies (eight magenta spectroscopic and 12 cyan photometric) that lie within the red circle centered on UMG 160748. "Field" galaxies are defined to be the 286 cyan galaxies that lie within the lower half of the DR3 footprint and the upper part of the far-right strip, i.e., below and to the right of the black dashed lines (Section 4.2).

between 7.0 and 10.1, and A_v between 0 and 5. The age of a galaxy was limited by the age of the universe at its redshift.

2.2. MAGAZ3NE Survey and UMGs 179370 and 160748

UMG ID "COS-DR3-179370" (hereafter 179370) and UMG ID "COS-DR3-160748" (hereafter 160748) are two members of a sample of UMGs and their environments at $3 < z < 4$ that we have been targeting for spectroscopic observations using the MOSFIRE spectrograph (McLean et al. 2010, 2012) on the W. M. Keck Observatory (PI Wilson). This sample of UMGs was selected photometrically from multi-passband optical-infrared catalogs of the COSMOS UltraVISTA (A. Muzzin et al. 2022, in preparation) and VIDEO fields (M. Annunziatella et al. 2022, in preparation). MOSFIRE spectra and stellar population properties (stellar mass, star formation rate, star formation history, quiescence) of the 16 MAGAZ3NE UMGs that have been spectroscopically confirmed to date were presented in Forrest et al. (2020b), including the discovery of the most massive spectroscopically confirmed quiescent UMG yet confirmed at $z > 3$ (Forrest et al. 2020a). A key goal of the MAGAZ3NE survey is to utilize MOSFIRE's powerful multiplexing capabilities in combination

Table 1
Overview of Observations

Mask	Observation date	Exposure time (s)	Seeing (FWHM)
A	2017 Nov 21	9304.8	0.″75
B	2017 Nov 22	7873.3	0.″73
C	2019 Mar 18	3578.0	0.″61

with the uniquely deep and extensive DR3 (and VIDEO) catalogs to characterize not only each UMG but also its environment.

UMG 179370 and 160748 were first identified as candidate UMGs at $3 < z < 4$ by Marchesini et al. (2010), based on analysis of the NEWFIRM Medium-Band Survey (NMBS; Whitaker et al. 2011). Marsan et al. (2017) presented spectroscopic confirmation of UMG 179370 (ID "C1-15182") by means of the [OIII]$\lambda\lambda$4959, 5007 doublet. Based on X-ray observations and line flux ratios, UMG 179370 contains a powerful AGN. UMG 179370 is estimated to have a star formation rate (SFR) of less than $100\,M_{\odot}\,\mathrm{yr}^{-1}$ based on UV-to-FIR SED fitting (Marsan et al. 2017) or alternatively, less than $15\,M_{\odot}\,\mathrm{yr}^{-1}$ based on its Hβ line flux (Forrest et al. 2020b).

Spectroscopic confirmation of UMG 160748, a poststarburst (PSB) galaxy, was first presented in Marsan et al. (2015), and it has since been studied further extensively [identified by ID "C1-23152" in Marsan et al. (2015) and Saracco et al. (2020), and "COS-DR3-160748" in Forrest et al. (2020b)]. Detailed analysis of its UV-to-FIR SED revealed that most of its stars formed at $z > 4$ in a highly dissipative, intense, and short burst of star formation. Based on its emission-line ratios, it also contains a powerful AGN. UMG 160748 has a star formation rate of less than $10\,M_{\odot}\,\mathrm{yr}^{-1}$ and has negligible dust extinction (Marsan et al. 2017; Saracco et al. 2020; Forrest et al. 2020b). The bulk of the stars in UMG 160748 appear to have supersolar metallicity and the dynamical mass estimated from the stellar velocity dispersion is consistent with the stellar mass derived from SED fitting (Saracco et al. 2020).

2.3. MOSFIRE Spectroscopic Observations and Data Reduction

As shown in Figure 1, two *K*-band masks (A and B) centered on UMG 179370 were observed in November 2017 and one *K*-band mask (C) centered on UMG 160748 was observed in March 2019. Filler slits were placed on DR3 targets with photometric redshift $z_{\mathrm{phot}} \pm 0.3$ of the UMG, with priority given to galaxies with total K_s-band magnitude brighter than $K_{s,\mathrm{tot}} = 23.0$. Exposure times ranged between 3500 and 9300 s. The observations are summarized in Table 1.

We began reduction by running the MOSFIRE Data Reduction Pipeline[10] (DRP) to obtain 2D target and error spectra. The DRP constructs a pixel flat image, identifies slits, removes thermal contamination, performs wavelength calibration using sky lines and neon arc lamps, removes sky background, and rectifies the spectrum.

We extracted the 1D spectra with a modified version of the MOSFIRE DRP designed to perform telluric corrections and mask sky lines (Forrest et al. 2020b). By visually inspecting the 2D spectrum, we determined whether stellar continuum or an emission feature was present. When stellar continuum was present, we collapsed the 2D spectrum along the wavelength axis to identify the location of the trace. A Gaussian was then fit to the collapsed spectrum and used as the weighting for optimal extraction (Horne 1986). When only an emission feature was present, we collapsed the spectrum along the limited portion of wavelength space containing the emission feature and between the nearest sky lines. We then applied a telluric correction using spectra of the science calibration stars, and masked regions with contamination from bright sky lines to obtain a final 1D extracted spectrum (see Forrest et al. 2020b). For objects that appeared in both masks A and B, we weighted the extracted 1D spectra and the noise spectra by the inverse variance and coadded them.

[10] https://github.com/Keck-DataReductionPipelines/MosfireDRP

2.4. Redshift Determination

For an emission-line galaxy at $z \sim 3.37$, Hβ and the [OIII] $\lambda\lambda$4959, 5007 doublet fall in the observed *K* band. In order to obtain a spectroscopic redshift we fit a three-Gaussian model to the emission features in the 1D extracted spectrum with six free parameters: redshift, the fluxes of the three lines, a line width (identical for all three lines), and a constant flux offset to account for the stellar continuum. When fitting the model to the [OIII]$\lambda\lambda$4959, 5007 doublet, we fit the fluxes of the emission lines independently, but the best fit generally resulted in a line ratio very close to the expected ratio of 1:3. We obtained spectroscopic redshifts for 14 galaxies including UMG 179370 from masks A and B, and eight galaxies including UMG 160748 from mask C (Table 2).

Figure 2 shows the K_s-band images (left), 2D and 1D *K*-band spectra (center), and SEDs (right) for the first three galaxies in Table 2 (Figure 6 shows the same but for all galaxies in Table 2). The black solid line shows the 1D spectrum smoothed over 5 pixels ($\sim$11 Å), weighted by the inverse variance. The light gray shading shows the error spectrum. The solid red line is the best-fit six-parameter model described above, while the dotted red vertical lines show the wavelengths corresponding to Hβ and [OIII]$\lambda\lambda$4959, 5007 at the best-fit spectroscopic redshift, z_{spec}.

The uncertainty on each spectroscopic redshift was obtained by adding statistical and systematic uncertainties in quadrature. In order to calculate the statistical uncertainty for each spectrum, 1000 simulated spectra were created by perturbing the flux at each wavelength of the observed spectrum by a Gaussian random amount with the standard deviation set by the level of the 1σerror spectrum. The 1000 simulated spectra were then fit to obtain a distribution of values for the redshift. Upper and lower 1σconfidence limits (i.e., the statistical uncertainty) were obtained by integrating the redshift probability distribution to find the 16th and 84th percentile values. On average, the statistical uncertainty obtained was $\delta z \sim 0.0002$.

The systematic error on the redshift was calculated by multiplying the spectral dispersion ($2.17\,\text{Å pixel}^{-1}$) by the pixel resolution (2.78 pixels), to obtain the spectral resolution (6.03 Å). At $z = 3.37$ this spectral resolution corresponds to $\delta z \sim 0.0012$. In every case, the systematic uncertainty dwarfed the statistical uncertainty.

The left panel of Figure 3 shows the excellent agreement between the spectroscopic and photometric redshifts. The blue and green stars indicate UMG 179370 and UMG 160748, and the blue and green squares show galaxies with spectroscopic redshifts near UMG 179370 (masks A and B) and UMG 160748 (mask C), respectively. Members with broader photometric redshift probability distributions have larger

Table 2
Properties of Spectroscopic Members of MAGAZ3NE J0959 (upper) and MAGAZ3NE J1000 (lower), Ordered by Stellar Mass

ID	Mask	R.A.	Decl.	K_s	$z_{\rm spec}$	C[a]	Stellar Mass $\log(M_\star/M_\odot)$	Age log(yr)	SFR $\log(M_\odot\ {\rm yr}^{-1})$
179370[b]	A, B	9h59m24.s3936	+2°25′36.″5117	22.14	3.3670 ± 0.0012	1	$11.37^{+0.04}_{-0.07}$	$9.0^{+0.1}_{-0.1}$	$0.50^{+0.59}_{-0.60}$
181529	A, B	9h59m10.s2576	+2°27′54.″0562	22.95	3.3701 ± 0.0013	1	$10.69^{+0.06}_{-0.04}$	$8.7^{+0.1}_{-0.1}$	$-0.35^{+0.81}_{-0.65}$
180562	A	9h59m11.s2104	+2°26′45.″7015	22.71	3.3624 ± 0.0012	1	$10.36^{+0.05}_{-0.00}$	$8.4^{+0.1}_{-0.1}$	$1.00^{+0.01}_{-0.08}$
180898	A	9h59m8.s2152	+2°27′10.″3471	22.34	3.3666 ± 0.0012	1	$10.34^{+0.11}_{-0.02}$	$8.3^{+0.1}_{-0.0}$	$1.08^{+0.02}_{-0.04}$
180419	A	9h59m21.s9552	+2°26′40.″1554	22.97	3.3650 ± 0.0012	2	$10.34^{+0.09}_{-0.01}$	$8.5^{+0.0}_{-0.1}$	$0.54^{+0.48}_{-0.13}$
180910	A	9h59m16.s1016	+2°27′12.″1205	22.78	3.3676 ± 0.0012	1	$10.32^{+0.03}_{-0.06}$	$8.5^{+0.0}_{-0.1}$	$1.33^{+0.19}_{-0.24}$
179810	A	9h59m17.s6304	+2°26′4.″3588	23.36	3.3270 ± 0.0012	1	$10.25^{+0.07}_{-0.03}$	$8.3^{+0.2}_{-0.0}$	$1.24^{+0.35}_{-0.12}$
181634	A	9h59m19.s1352	+2°27′59.″7582	22.87	3.3696 ± 0.0012	1	$10.21^{+0.06}_{-0.03}$	$8.5^{+0.0}_{-0.1}$	$1.02^{+0.03}_{-0.04}$
181058	B	9h59m21.s7272	+2°27′23.″5634	23.84	3.3287 ± 0.0013	3	$10.13^{+0.03}_{-0.11}$	$8.4^{+0.1}_{-0.1}$	$1.04^{+0.20}_{-0.48}$
181039	A	9h59m14.s7624	+2°27′22.″3693	23.62	3.3661 ± 0.0012	2	$10.05^{+0.04}_{-0.05}$	$8.4^{+0.0}_{-0.1}$	$0.69^{+0.34}_{-0.21}$
180737	B	9h59m11.s0640	+2°27′2.″5391	23.79	3.3622 ± 0.0012	1	$9.86^{+0.11}_{-0.08}$	$8.6^{+0.2}_{-0.1}$	$1.03^{+0.10}_{-0.13}$
180577	A, B	9h59m12.s4320	+2°26′50.″5907	24.33	3.3707 ± 0.0013	3	$9.86^{+0.07}_{-0.14}$	$8.6^{+0.1}_{-0.2}$	$0.58^{+0.30}_{-0.43}$
179570	B	9h59m18.s2304	+2°25′51.″8840	24.36	3.3272 ± 0.0012	3	$9.72^{+0.15}_{-0.05}$	$8.5^{+0.1}_{-0.1}$	$-0.08^{+0.67}_{-0.21}$
180993	A	9h59m13.s0872	+2°27′20.″5978	24.80	3.3646 ± 0.0012	1	$8.99^{+0.17}_{-0.14}$	$8.1^{+0.2}_{-0.4}$	$0.36^{+0.1}_{-0.28}$
160748[b]	C	10h0m27.s8112	+2°33′49.″2289	20.26	3.3520 ± 0.0012	1	$11.47^{+0.03}_{-0.03}$	$8.6^{+0.0}_{-0.1}$	$0.49^{+0.03}_{-0.03}$
158792	C	10h0m18.s8880	+2°32′1.″0410	22.50	3.4136 ± 0.0012	1	$10.68^{+0.03}_{-0.05}$	$8.6^{+0.0}_{-0.1}$	$1.39^{+0.25}_{-0.06}$
160752	C	10h0m36.s4296	+2°33′53.″6620	21.85	3.4261 ± 0.0012	1	$10.53^{+0.05}_{-0.05}$	$8.3^{+0.0}_{-0.1}$	$1.72^{+0.09}_{-0.15}$
158809	C	10h0m34.s5120	+2°32′2.″2290	22.83	3.3910 ± 0.0012	1	$10.34^{+0.03}_{-0.02}$	$8.4^{+0.0}_{-0.1}$	$0.64^{+0.02}_{-0.12}$
158027	C	10h0m22.s8432	+2°31′17.″6844	22.72	3.4176 ± 0.0012	3	$10.30^{+0.07}_{-0.02}$	$8.6^{+0.1}_{-0.1}$	$1.02^{+0.02}_{-0.04}$
158806	C	10h0m29.s9016	+2°32′3.″7946	23.56	3.3509 ± 0.0012	2	$10.02^{+0.07}_{-0.04}$	$8.8^{+0.0}_{-0.1}$	$0.90^{+0.01}_{-0.09}$
158838	C	10h0m29.s1840	+2°32′5.″3916	24.55	3.3493 ± 0.0012	2	$9.54^{+0.07}_{-0.11}$	$8.5^{+0.1}_{-0.2}$	$0.35^{+0.05}_{-0.31}$
160549	C	10h0m27.s0312	+2°33′48.″3826	24.70	3.3572 ± 0.0012	1	$9.42^{+0.11}_{-0.12}$	$8.5^{+0.2}_{-0.2}$	$0.58^{+0.18}_{-0.24}$

Notes.
[a] The spectroscopic redshift confidence level was assigned based on the number of emission lines observed. A spectrum where two emission lines were observed, e.g., Hβ, or one or both lines of the [OIII]$\lambda\lambda$4959, 5007 doublet, was assigned a confidence level of 1, a spectrum where a single high S/N emission line (S/N $\geqslant$ 3) was observed was assigned a confidence level of 2, and a spectrum where a single low S/N (S/N < 3) emission line was observed was assigned a confidence level of 3.
[b] UMG (primary target).

photometric redshift uncertainties. The median of the scatter in $|z_{\rm spec} - z_{\rm phot}|/(1 + z_{\rm spec})$ is 0.0058.

We obtained spectroscopic redshifts for 22 galaxies in the redshift range $3.2 < z < 3.5$ (including both UMGs). In order to derive more accurate estimates of stellar mass, star formation rate, and age for those 22 galaxies shown in Table 2, we fixed $z = z_{\rm spec}$ and then reran FAST (Kriek et al. 2009) on the DR3 catalog using the same parameters as in Section 2.1.

3. Protocluster Membership

3.1. Spectroscopic Members

The right panel of Figure 3 shows a histogram of the galaxies with spectroscopic redshifts close to that of UMG 179370 (upper; blue) and to that of UMG 160748 (lower; green). The redshifts of the UMGs are shown by the dashed black lines. We consider the 22 galaxies with line-of-sight velocities within $\pm 6000\ {\rm km\ s^{-1}}$ ($\Delta z = 0.0874$) of each of the UMGs (red dashed lines) to be spectroscopic members. There are 14 spectroscopic members (including UMG 179370) of protocluster MAGAZ3NE J095924+022537 (hereafter J0959) and eight spectroscopic members (including UMG 160748) of protocluster MAGAZ3NE J100028+023349 (hereafter J1000). In naming each protocluster, the R.A. and decl. was chosen to coincide with the coordinates of its UMG. The positions of the 22 spectroscopic protocluster members are shown by magenta crosses in Figure 1. The $\pm 6000\ {\rm km\ s^{-1}}$ velocity cut used here is similar to that used to determine spectroscopic membership for other high-redshift protoclusters (Lemaux et al. 2014) and is well matched to the redshift extent of simulated protostructures (Chiang et al. 2013; Muldrew et al. 2015).

Using the biweight location estimator (Beers et al. 1990), we determined the mean redshift of the 14 spectroscopically confirmed members of MAGAZ3NE J0959 to be $z = 3.3665^{+0.0009}_{-0.0012}$ and the mean redshift of the eight members of MAGAZ3NE J1000 to be $z = 3.3801^{+0.0213}_{-0.0281}$. The uncertainties on the mean redshifts were calculated using bootstrapping.

3.2. Photometric Members

There are 236,196 objects in the DR3 catalog. In order to determine photometric membership for the two protoclusters, we began by fitting each of the galaxies in the DR3 catalog with EAZY (Brammer et al. 2008) to derive a best-fit photometric redshift, $z_{\rm peak}$, and with FAST (Kriek et al. 2009) to derive the stellar mass and star formation rate. Simulations have shown that the DR3 catalog is 90% complete down to a total K_s-band magnitude of $K_{s,{\rm tot}} = 24.5$, and that this corresponds to a 95% completeness above a stellar mass of $\log(M_\star/M_\odot) = 10.5$ at $z \sim 4$ (A. Muzzin et al. 2022, in preparation). We, therefore, selected those galaxies with $K_s \leqslant 24.5$ and $\log(M_\star/M_\odot) \geqslant 10.5$, and also made an initial photometric selection of $2.75 < z_{\rm peak} < 4$. There were 1279 galaxies that satisfied those three criteria.

Next we wished to select the members of the "slice" centered on MAGAZ3NE J0959. In determining membership,

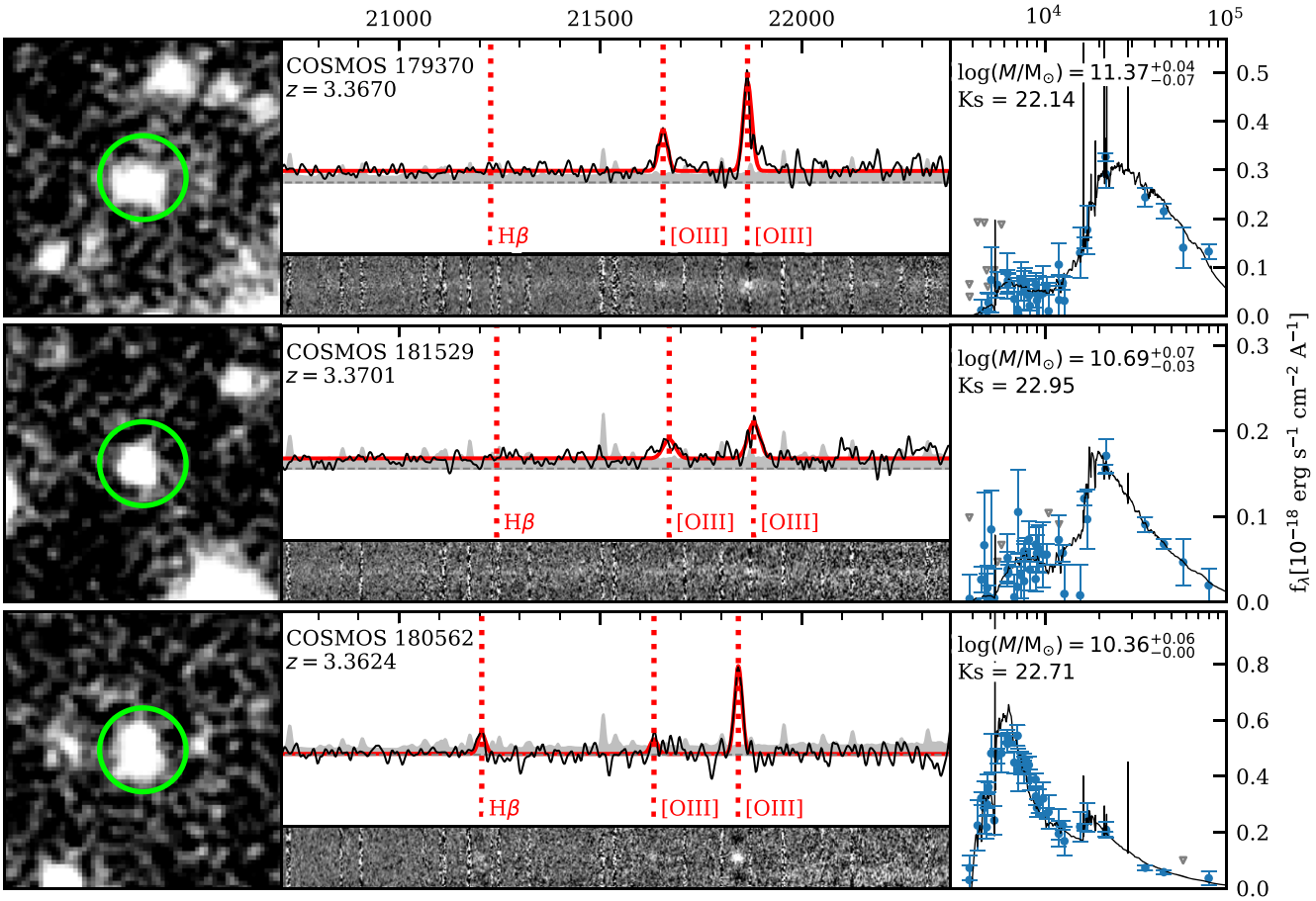

Figure 2. K_s-band image (left), MOSFIRE 1D K-band spectra (upper center), MOSFIRE 2D K-band spectra (lower center), and the SED (right) of spectroscopically confirmed members (the first three members of Table 2 are shown here; all 22 members are shown in Figure 6). The black solid line shows the spectrum smoothed over 5 pixels weighted by the inverse variance. The light gray shading shows the magnitude of the error spectrum and the horizontal dashed dark gray line indicates where the flux is zero. The solid red line is the best-fit six-parameter model described in Section 2.4. The vertical red dotted lines show the position at which Hβ and [OIII]$\lambda\lambda$4959, 5007 doublet emission lines would appear at the spectroscopic redshift of each galaxy. The photometric fluxes and their 1σerrors are shown on the right in blue, with the best-fit SED shown in black. For those bands for which the flux is negative, the 3σ upper limit is shown as a gray downward-pointing triangle.

photometric analyses often simply select galaxies with $z_{\rm phot}$ within a given redshift range. However, this does not take account of the fact that each galaxy has a different redshift probability distribution function, $p(z)$. Therefore here, to account for the diversity in the $p(z)$ distributions, we instead adopted a probabilistic selection applied to each galaxy in turn. We integrated $p(z)$ for each galaxy using the redshift of protocluster MAGAZ3NE J0959 as the fiducial central redshift, and the median photometric uncertainty of the sample of 1279 galaxies $\Delta z_{\rm phot,sample}$ as the lower and upper limits:

$$P = \frac{\int_{z_{\rm J0959}-\Delta z_{\rm phot,sample}}^{z_{\rm J0959}+\Delta z_{\rm phot,sample}} p(z)dz}{\int_0^\infty p(z)dz}. \quad (1)$$

Galaxies with an integrated probability P in excess of a threshold probability $P_{\rm thresh}$ will be considered members of the protocluster redshift slice. We explain below in detail how we calculated the actual values of $\Delta z_{\rm phot,sample}$ and $P_{\rm thresh}$ ($\Delta z_{\rm phot,sample} = 0.2$ and $P_{\rm thresh} = 0.17$). However, we note that we utilized different values of $\Delta z_{\rm phot,sample}$ (in the range $0.10 \leqslant \Delta z_{\rm phot,sample} \leqslant 0.3$) and $P_{\rm thresh}$ (in the range $0.15 \leqslant P_{\rm thresh} \leqslant 0.5$), and any choice of value in those ranges had minimal impact on the number of protocluster members or the quiescent fraction results presented in Section 4.2.

In general, the precision of any sample of photometric redshifts is often expressed as a percentage, $\Delta z_{\rm phot,sample}/(1 + z_{\rm phot})$. For this sample of 1279 galaxies, we calculated the median percentage to be 4.5% by determining $\Delta z_{\rm phot,galaxy}/(1 + z_{\rm phot})$ for each galaxy using the 16th and 84th percentile values of its $p(z)$ distribution output by EAZY as that galaxy's photometric redshift uncertainty $\Delta z_{\rm phot,galaxy}$. In other words, the median photometric redshift uncertainty expressed as a function of redshift is $\Delta z_{\rm phot,sample} = 0.045(1 + z_{\rm phot})$, and at the redshift of MAGAZ3NE J0959, $\Delta z_{\rm phot,sample} \sim 0.2$. Having calculated the value of $\Delta z_{phot,\rm sample}$ (used in the integration limits in Equation (1)), we then calculated the integrated probability P for each galaxy using Equation (2):

$$P = \frac{\int_{z_{\rm J0959}-0.2}^{z_{\rm J0959}+0.2} p(z)dz}{\int_0^\infty p(z)dz} = \frac{\int_{3.167}^{3.567} p(z)dz}{\int_0^\infty p(z)dz}. \quad (2)$$

To determine the threshold value, $P_{\rm thresh}$, we consider a hypothetical galaxy that has a Gaussian $p(z)$ with an uncertainty

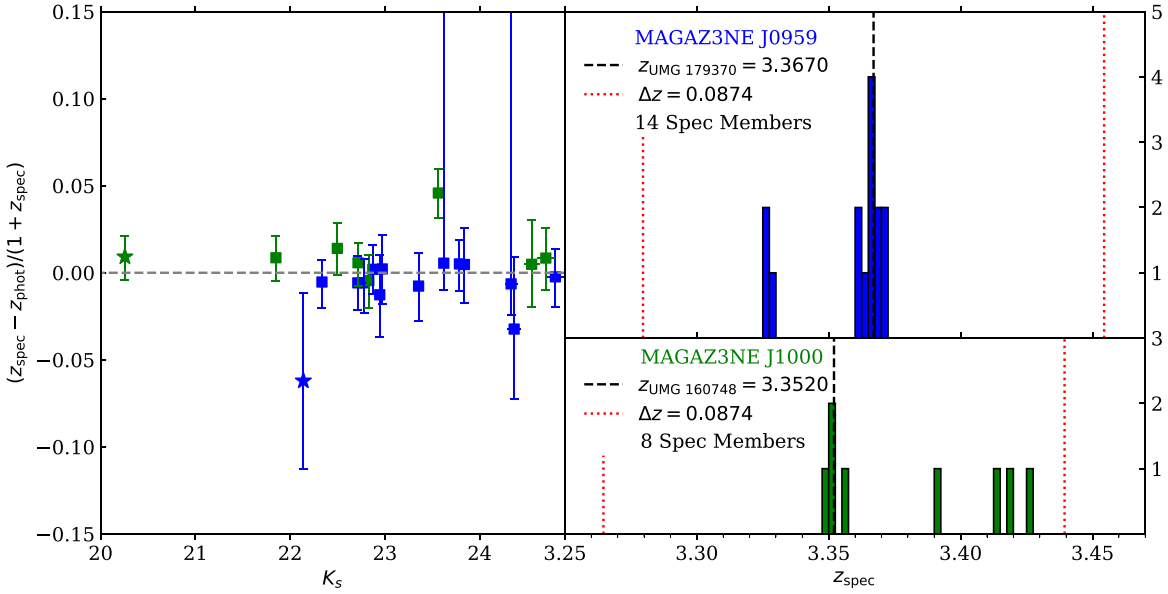

Figure 3. Left: blue and green symbols show the 22 spectroscopic members of protocluster MAGAZ3NE J0959 (upper right) and protocluster MAGAZ3NE J1000 (lower right). The blue and green stars indicate UMG 179370 and UMG 160748, respectively. There is excellent agreement between the spectroscopic and photometric redshifts for the 22 spectroscopic members (members with broader photometric redshift probability distributions have larger photometric redshift uncertainties). Right: histograms of the spectroscopic members shown at left (with properties summarized in Table 2). The upper panel shows galaxies with spectroscopic redshifts close to UMG 179370 (masks A and B in Table 1) and the lower panel shows UMG 160748 (mask C in Table 1). The redshifts of the two UMGs are shown by the dashed black lines. We consider the 22 galaxies with velocities within ± 6000 km s^{-1} ($\Delta z = 0.0874$) of each of the UMGs (red dashed lines) to be spectroscopic protocluster members. Those galaxies are indicated by magenta crosses in Figure 1.

of three times the median photometric redshift uncertainty, $\Delta z_{\rm phot,sample}$. We would like this galaxy to fall just at the $P_{\rm thresh}$ limit for inclusion in the redshift slice. To achieve this we set the photometric redshift of this hypothetical galaxy such that the redshift of MAGAZ3NE J0959 fell at this galaxy's photometric redshift uncertainty (i.e., $z_{\rm phot} \pm \Delta z_{\rm phot,galaxy} = z_{\rm J0959}$). By applying Equation (2) to this hypothetical galaxy, we obtained $P = 0.17$ which we then adopt to be the threshold probability $P_{\rm thresh}$. Each of the 1279 galaxies in our sample with $P \geqslant P_{\rm thresh}$ are considered to be members of the redshift slice. We note that we experimented with using different values of $P_{\rm thresh}$ (in the range $0.15 \leqslant P_{\rm thresh} \leqslant 0.5$) but once again found any choice of value in this range to have minimal impact on the number of protocluster members or the quiescent fraction results presented in Section 4.2.

The cyan circles in Figure 1 show the remaining 550 galaxies that have $P \geqslant 0.17$, each with its size scaled by its P value (galaxies that are spectroscopic members are assigned $P = 1$). The smoothed density map in Figure 1 was generated by applying a Gaussian kernel density estimator to the 550 galaxies weighted by their P value, with maximal density colored yellow, and contours are drawn at 20% intervals of the maximum value. We chose a kernel bandwidth of 7.′7 ($\sim$15 comoving Mpc), which approximately corresponds to the predicted physical size of a massive protocluster at this redshift. The contours and smoothed density map, which are shown in Figure 1, have been truncated at the edges of the ultra-deep stripes.

Simulations have shown that 10 comoving Mpc is approximately equal to the Lagrangian radius at $z \sim 3.37$ (Chiang et al. 2017). As a final step in determining photometric membership, we retained only those galaxies within a radius of 10 comoving Mpc from each UMG. This selection resulted in a total of 26 photometric members for MAGAZ3NE J0959 (two photometric members of which, UMG 179370 and galaxy ID "181529" were also independently spectroscopically confirmed). This selection also resulted in a total of 15 photometric members for MAGAZ3NE J1000 (three photometric members of which UMG 160748 and galaxy IDs "158792" and "160752" were also independently spectroscopically confirmed). We note that most of the spectroscopically confirmed members of the two protoclusters are emission-line galaxies with stellar masses below the completeness limit of the photometric catalog (Table 1). As a result, these galaxies were not identified as photometric members despite otherwise having photometric redshifts consistent with membership.

4. UVJ Classification and Quiescent Fraction

4.1. Rest-frame Colors and UVJ Classification

The *UVJ* diagram has become an established method for separating quiescent from star-forming galaxies (Wuyts et al. 2007; Williams et al. 2009). Rest-frame $U - V$ and $V - J$ colors were calculated for the 22 spectroscopic members (Section 3.1) by setting $z = z_{\rm spec}$ and using EAZY (Brammer et al. 2008). Uncertainties for these colors for each galaxy were calculated by perturbing the flux in each band 10,000 times. The amplitude of the perturbation in each band was determined by sampling from a normal distribution centered on the observed value of flux with width, σ, equal to the uncertainty in the flux measurement. Each perturbed SED was then fit with EAZY, obtaining a distribution of $U - V$ and $V - J$ rest-frame colors. The 16th and 84th percentile values of that distribution were taken to be the uncertainty in the color for that galaxy.

Figure 4 shows rest-frame $U - V$ and $V - J$ colors for MAGAZ3NE J0959 (left) and MAGAZ3NE J1000 (right). UMG 179370 is shown by a blue star and UMG 160748 by a green star. The 20 other spectroscopically confirmed members of MAGAZ3NE J0959 and MAGAZ3NE J1000 are shown as solid blue and solid green circles, respectively. The open blue

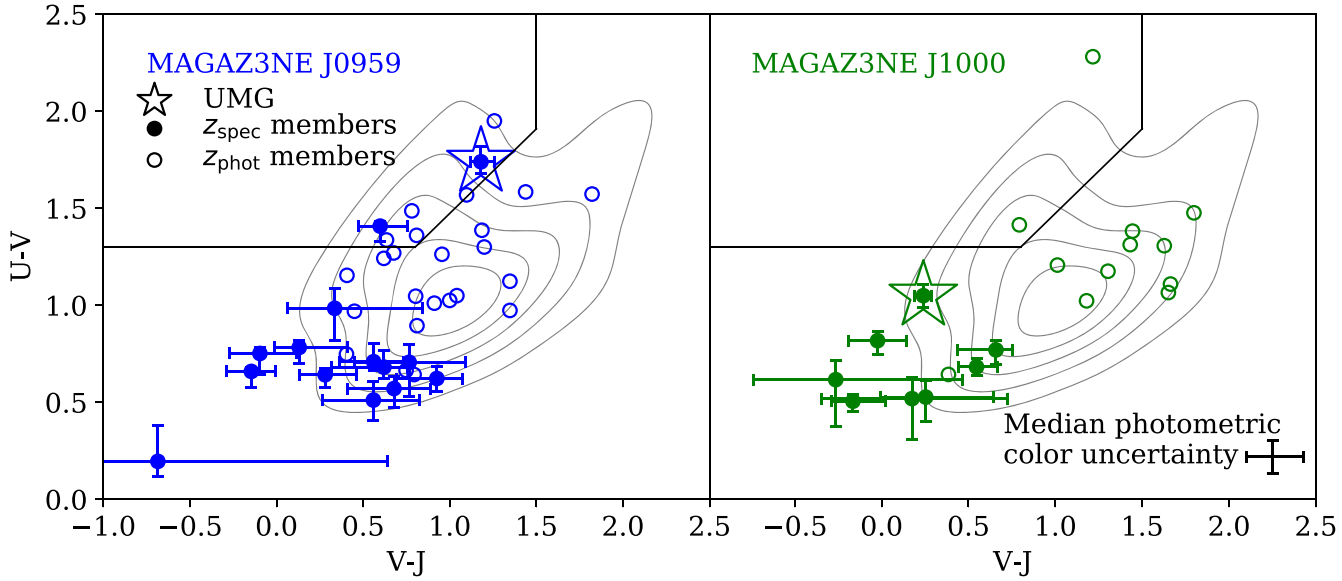

Figure 4. *UVJ* color–color diagram for MAGAZ3NE J0959 (left) and MAGAZ3NE J1000 (right). UMG 179370 is shown by the blue star and UMG 160748 by the green star. The 13 (7) additional spectroscopic members and 24 (12) photometric members of MAGAZ3NE J0959 (MAGAZ3NE J1000) are shown by solid and open blue (green) circles. The black cross at the bottom right shows the median uncertainty in the colors of the photometric members. Note that most of the spectroscopically confirmed members of the two protoclusters were not identified as photometric members because they are emission-line galaxies that fall below the stellar mass completeness limit ($\log(M_\star/M_\odot) = 10.5$) applied to the DR3 catalog. Only one spectroscopically confirmed member, other than the UMGs, has a stellar mass greater than $\log(M_\star/M_\odot) = 10.5$ (ID "81529" in Table 2). The contours show the field sample (defined in Section 4.2), and the wedge defined by the solid black lines shows the quiescent galaxy selection criteria proposed by Whitaker et al. (2011). Interestingly, as shown in the left panel, UMG 179370 (and galaxy 181529) are *UVJ* quiescent. In contrast, because UMG 160748's star formation quenched rather recently and abruptly (within the last few hundred Myr; Marsan et al. 2015, 2017; Saracco et al. 2020; Forrest et al. 2020b), it still has blue *UVJ* colors but is expected to move up into the quiescent bin in the next few hundred Myr.

Table 3
Quiescent Fractions for Protocluster MAGAZ3NE J0959 and Field

Stellar Mass	Protocluster QF (%) (Background corrected)	Protocluster QF (%) (Uncorrected)	Field QF (%)	# Protocluster Q/SF	# Field Q/SF
$10.5 \leqslant \log(M_\star/M_\odot) < 10.85$	$1.1^{+18.8}_{-1.1}$	$6.2^{+12.9}_{-5.2}$	$17.3^{+3.1}_{-2.7}$	1/15	35/167
$10.85 \leqslant \log(M_\star/M_\odot) < 11.2$	$70.9^{+29.1}_{-16.8}$	$57.1^{+22.3}_{-24.6}$	$16.9^{+5.7}_{-4.6}$	4/3	12/59
$11.2 \leqslant \log(M_\star/M_\odot) < 11.55$	$74.8^{+25.2}_{-15.1}$	$66.7^{+27.7}_{-41.3}$	$0.0^{+13.2}_{-0.0}$	2/1	0/13
$10.5 \leqslant \log(M_\star/M_\odot) < 11.0$	$19.8^{+17.7}_{-7.4}$	$19.0^{+12.5}_{-8.9}$	$17.3^{+2.8}_{-2.5}$	4/17	42/201
$11.0 \leqslant \log(M_\star/M_\odot) < 11.55$	$73.3^{+26.7}_{-16.9}$	$60.0^{+25.3}_{-30.3}$	$11.6^{+7.1}_{-4.9}$	3/2	5/38

circles show the 24 galaxies classified as photometric members of MAGAZ3NE J0959, and the open green circles show the 12 galaxies classified as photometric members of MAGAZ3NE J1000 (Section 3.2).

Also plotted in Figure 4 is the quiescent selection criteria proposed by Whitaker et al. (2011). Notably, UMG 179370 (MAGAZ3NE J0959) is *UVJ*quiescent, which is consistent with the low levels of star formation estimated from its Hβ line flux and from UV-to-FIR SED fitting (Section 2.2). To our knowledge, there are only two protoclusters above $z > 3$ in which the brightest (and most massive) galaxy is both spectroscopically confirmed and *UVJ*quiescent. These are the SSA22 protocluster at $z = 3.09$ (Kubo et al. 2021) and MAGAZ3NE J0959 at $z = 3.37$.

Other than UMG 179370, only one other spectroscopically confirmed member of protocluster MAGAZ3NE J0959 has a stellar mass more massive than $\log(M_\star/M_\odot) = 10.5$. This is galaxy "181529" in Table 2 (see also Section 3.1). Interestingly, as for UMG 179370, galaxy 181529 is *UVJ* quiescent (solid blue circle in the quiescent wedge in Figure 4).

In contrast, the UMG of MAGAZ3NE J1000 (UMG 160748) falls in the poststarburst region of the *UVJ* color–color diagram. This is consistent with its stellar population determined from NIR spectroscopy (Marsan et al. 2017; Saracco et al. 2020). Both UMG 179370 and UMG 160748 appear to have undergone rapid star formation quenching within the last 300 Myr (Saracco et al. 2020; Forrest et al. 2020b). Because UMG 160748's star formation quenched so recently and abruptly, it still has blue *UVJ* colors (Figure 4), but it is expected to transition into the quiescent wedge within the next few hundred Myr (Marsan et al. 2017; Merlin et al. 2018; Belli et al. 2019).

4.2. Quiescent Fraction of MAGAZ3NE J0959

We calculated the quiescent fraction (QF) for MAGAZ3NE J0959 and also for the field, i.e., the ratio of the number of quenched galaxies to the total number of galaxies:

$$\mathrm{QF} = \frac{N^{\mathrm{Q}}}{N^{\mathrm{Q}} + N^{\mathrm{SF}}}. \quad (3)$$

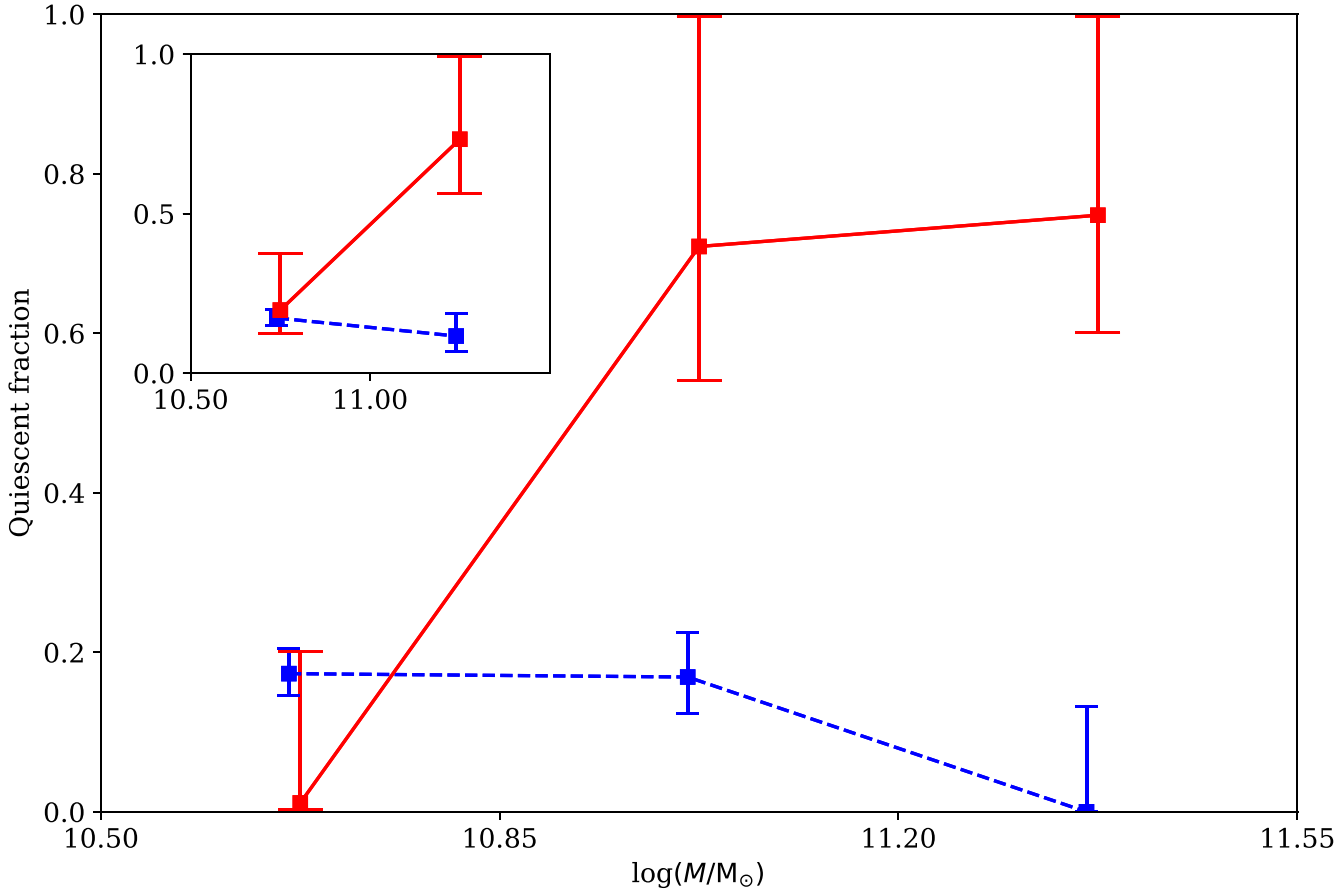

Figure 5. Quiescent fraction for protocluster MAGAZ3NE J0959 (solid red line) and field (dashed blue line) as a function of stellar mass for three mass intervals (two slightly different mass intervals are shown in the inset). The protocluster quiescent fraction shown in the figure is the quiescent fraction in excess of the field, i.e., the field fraction has been subtracted from the "raw" protocluster fraction (see Section 4.2 and Table 3 for details). The quiescent fraction in MAGAZ3NE J0959 exceeds that of the field, certainly at $\log(M_\star/M_\odot) \gtrsim 11.0$, and may also be mass dependent, increasing with stellar mass.

We calculated the QF only above the DR3 95% stellar mass completeness limit of $\log(M_\star/M_\odot) = 10.5$. As described in Section 3.2, there are 26 members of MAGAZ3NE J0959 (two spectroscopic and 24 photometric) within a 10 comoving Mpc radius (red circle) of UMG 179370, above this stellar mass completeness limit. As noted previously, most of the spectroscopically confirmed protocluster members are emission-line galaxies that fall below the stellar mass completeness limit and so are not included here in our determination of the QF.

We defined the region constituting the "field" to be the lower half of the DR3 footprint and the upper part of the right strip, i.e., the region below and to the right of the black dashed lines in Figure 1. This region was selected because we deemed it least likely to contain any members of the extended MAGAZ3NE J0959/J1000 protocluster system as indicated from the galaxy density contours for the entire COSMOS UltraVISTA field shown in Figure 1. Of the 550 galaxies determined photometrically to lie within the redshift slice centered on UMG 179370 (Section 3.2; shown by the cyan circles in Figure 1), a total of 286 lie within these two regions and comprise the field sample. The contours in Figure 4 show the distribution of field galaxies in *UVJ* color–color space.

Next we classified each galaxy in protocluster MAGAZ3NE J0959 and in the field either as quiescent or star forming based on its position in the *UVJ* diagram (Figure 4). As Table 3 shows, of the 26 members of MAGAZ3NE J0959, seven are quiescent and 19 are star forming, and of the 286 field galaxies, 47 are quiescent and 239 are star forming.

The dashed blue lines in Figure 5 show the field QF calculated using Equation (3) as a function of stellar mass for three mass intervals (two slightly different mass intervals are shown in the inset). The values are given in Table 3. In order to calculate uncertainties on the field QF, we sampled the Poisson distribution for the observed number of quenched galaxies and star-forming galaxies one million times. This was done for each stellar mass bin, enabling us to construct a distribution of quiescent fractions from which we took the 16th and 84th percentile values to be the uncertainty on the field QF. The uncertainties we calculated on the field QF are consistent with those found from analytic approximations (e.g., Gehrels 1986). We also find that our calculated field QF is in good agreement with measurements of the field at $3 < z < 4$ from the UltraVISTA DR1 catalog (Muzzin et al. 2013).

In order to calculate the protocluster QF, it was necessary to make a correction for contamination by foreground/background field galaxies that had been scattered into the protocluster redshift slice because of redshift uncertainties. The corrected protocluster quiescent fraction was calculated as

$$\mathrm{QF}_{\mathrm{corr}} = \frac{N_{\mathrm{PC}}^{\mathrm{Q}} - N_{\mathrm{F}}^{\mathrm{Q}}(A_{\mathrm{PC}}/A_{\mathrm{F}})}{N_{\mathrm{PC}}^{\mathrm{Q}} - N_{\mathrm{F}}^{\mathrm{Q}}(A_{\mathrm{PC}}/A_{\mathrm{F}}) + N_{\mathrm{PC}}^{\mathrm{SF}} - N_{\mathrm{F}}^{\mathrm{SF}}(A_{\mathrm{PC}}/A_{\mathrm{F}})}, \quad (4)$$

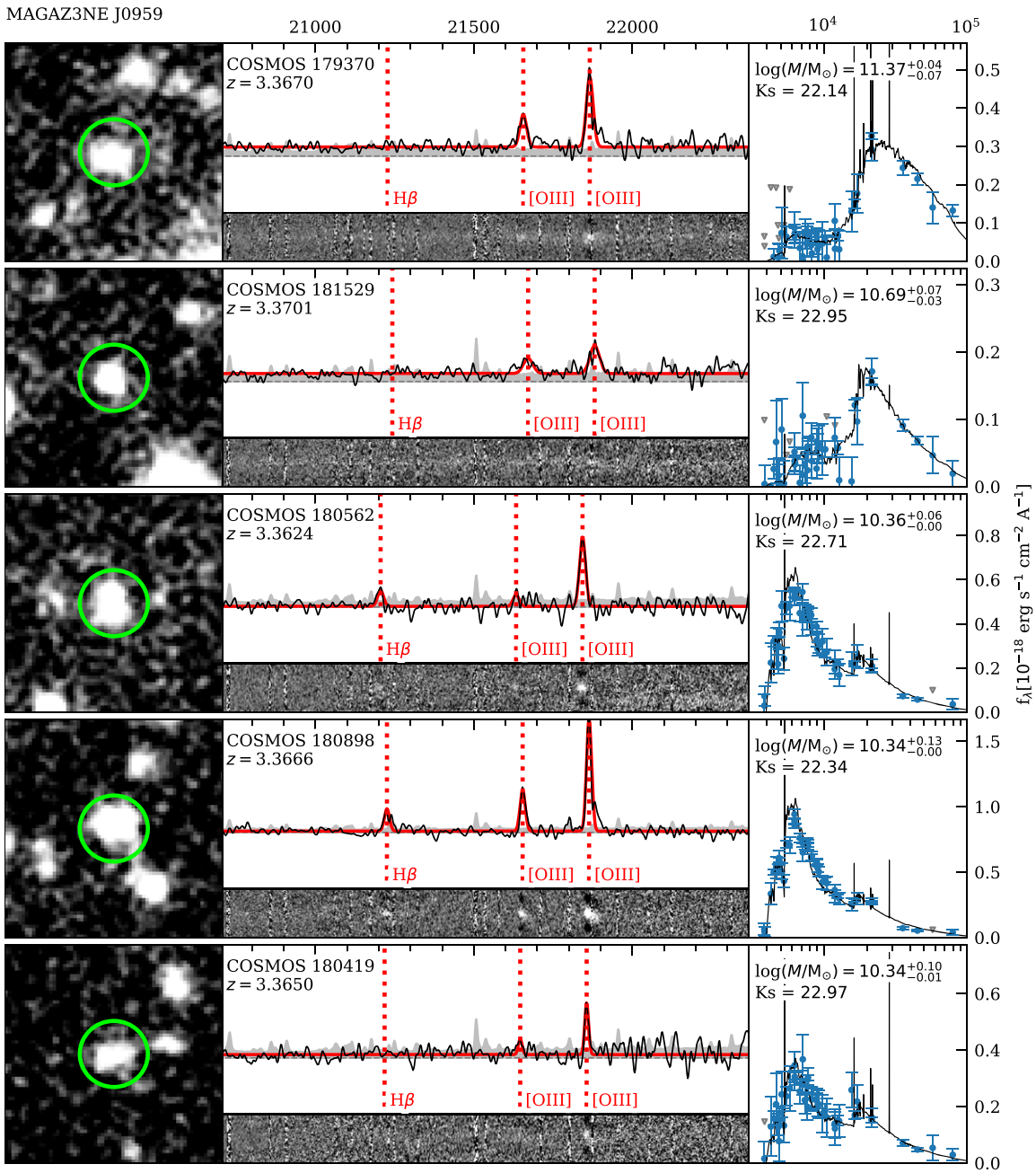

Figure 6. As for Figure 2 but for all 22 members, shown in the same order as in Table 2.

where $N_{\rm PC}^{\rm Q}$ was the number of quiescent galaxies in the protocluster, $N_{\rm F}^{\rm SF}$ was the number of star-forming galaxies in the field, and $A_{\rm PC}/A_{\rm F}$ was the ratio of the area of the protocluster to the area of the field. The solid red lines in Figure 5 show the protocluster QF as a function of stellar mass. Uncertainties on the protocluster QF were calculated in a similar manner to those of the field, with the additional step of background subtraction as shown in Equation (4). As we did for the field, we sampled the Poisson distribution for the observed number of quenched and star-forming galaxies in the protocluster. Then the number of quiescent and star-forming galaxies in the field were subtracted from the protocluster, scaled by area. Finally we calculated the fraction of quiescent systems in the resultant protocluster sample. The uncertainty on the protocluster QF was taken to be the 16th and 84th percentile values of the resulting distribution.

It is apparent from Figure 5 that the QF in MAGAZ3NE J0959 exceeds that of the field, certainly at $\log(M_\star/M_\odot) \gtrsim 11.0$, and may also be mass dependent, increasing with increasing stellar mass. We experimented with different *UVJ* criteria for selecting quiescent and star-forming galaxies, such as the one suggested in Martis et al. (2016) and also with centering the protocluster on the peak of the density map in Figure 1 rather than the UMG, but found the QF to be robust to those choices. We also calculated the QF for MAGAZ3NE J1000, but found that protocluster to have a QF much more similar to the field.

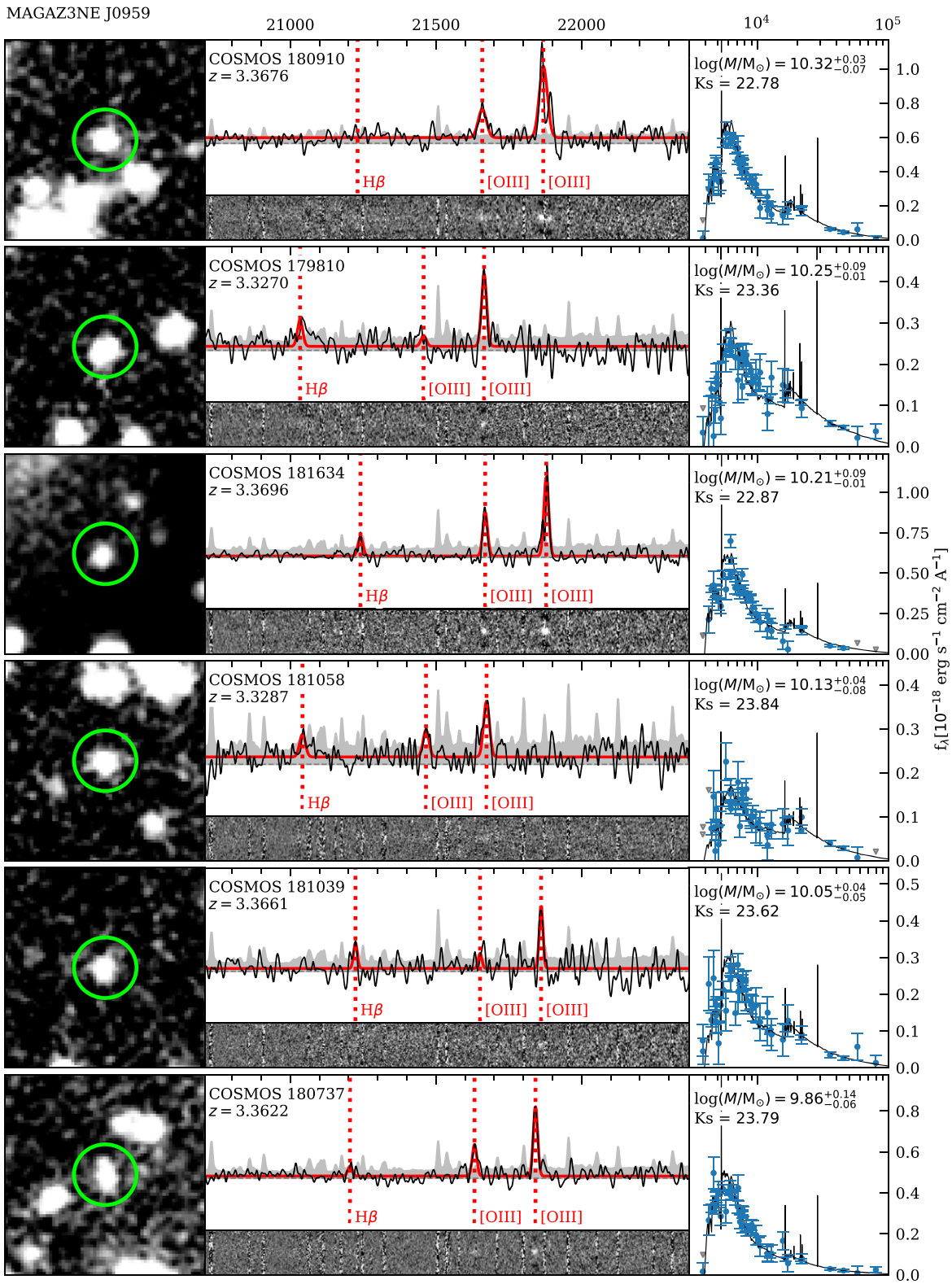

Figure 6. (Continued.)

5. Discussion

5.1. Star Formation and Quenching in Protoclusters

The existence of such a high QF in MAGAZ3NE J0959 is in marked contrast to the many known examples of protoclusters that are filled with star-forming galaxies (Chapman et al. 2009; Clements et al. 2014; Dannerbauer et al. 2014; Casey et al. 2015; Hung et al. 2016; Forrest et al. 2017; Miller et al. 2018; Cheng et al. 2019). There are a small number of protoclusters that have previously been reported as having an excess of massive, older, or quenched galaxies relative to the field, e.g., the $z = 2.30$ protocluster in the field of the bright $z = 2.72$ QSO HS 1700+643

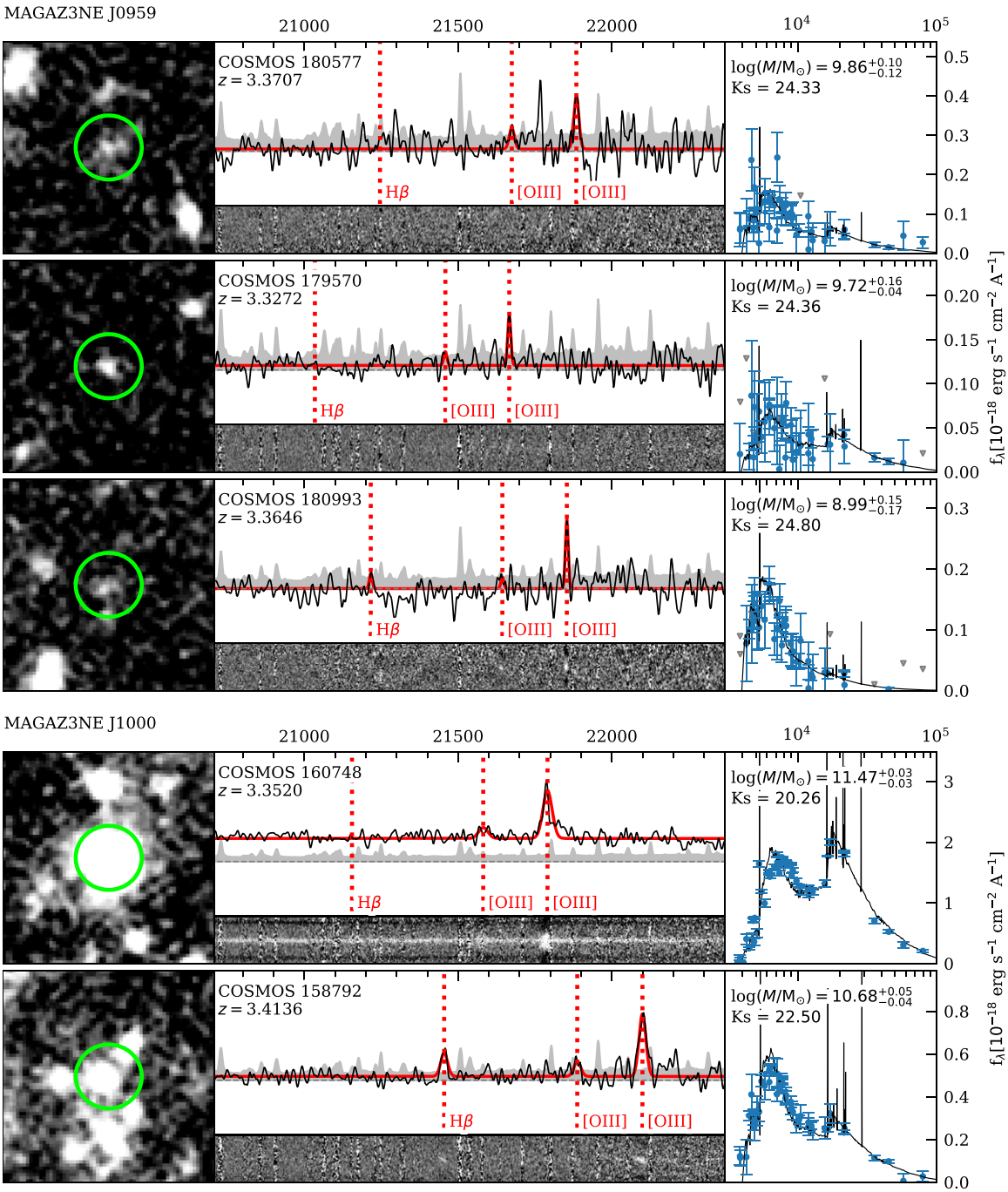

Figure 6. (Continued.)

(Steidel et al. 2005; Shapley et al. 2005), the SSA22 protocluster at $z = 3.09$ (Kubo et al. 2021), D4UD01 at $z = 3.24$ (Shi et al. 2021), and PC 217.96+32.3 at $z = 3.78$ (Shi et al. 2019). The discovery of MAGAZ3NE J0959 presented here provides another important counterexample to the suggestion that star-forming or even starbursting galaxies are ubiquitous in protoclusters at $z > 2$ (Casey 2016). The high QF observed in MAGAZ3NE J0959 serves to reinforce the viewpoint, instead, that protoclusters exist in a diversity of evolutionary states in the early universe, and that some systems have quenched remarkably early in the universe's history.

The high QF in MAGAZ3NE J0959 raises many interesting questions, not least of which is how the observed quenching has occurred. A recent analysis of the stellar mass functions (SMFs) of star-forming and quiescent galaxies in a sample of clusters at $1 < z < 1.5$ from the GOGREEN survey (van der Burg et al. 2020; see also Webb et al. 2020), returned two surprising results. First, the shapes of the SMFs were identical between cluster and field to high statistical precision, albeit with different normalizations. second, in stark contrast to the mass-independent environmental quenching observed in the local universe (Peng et al. 2010), the observed quenching was

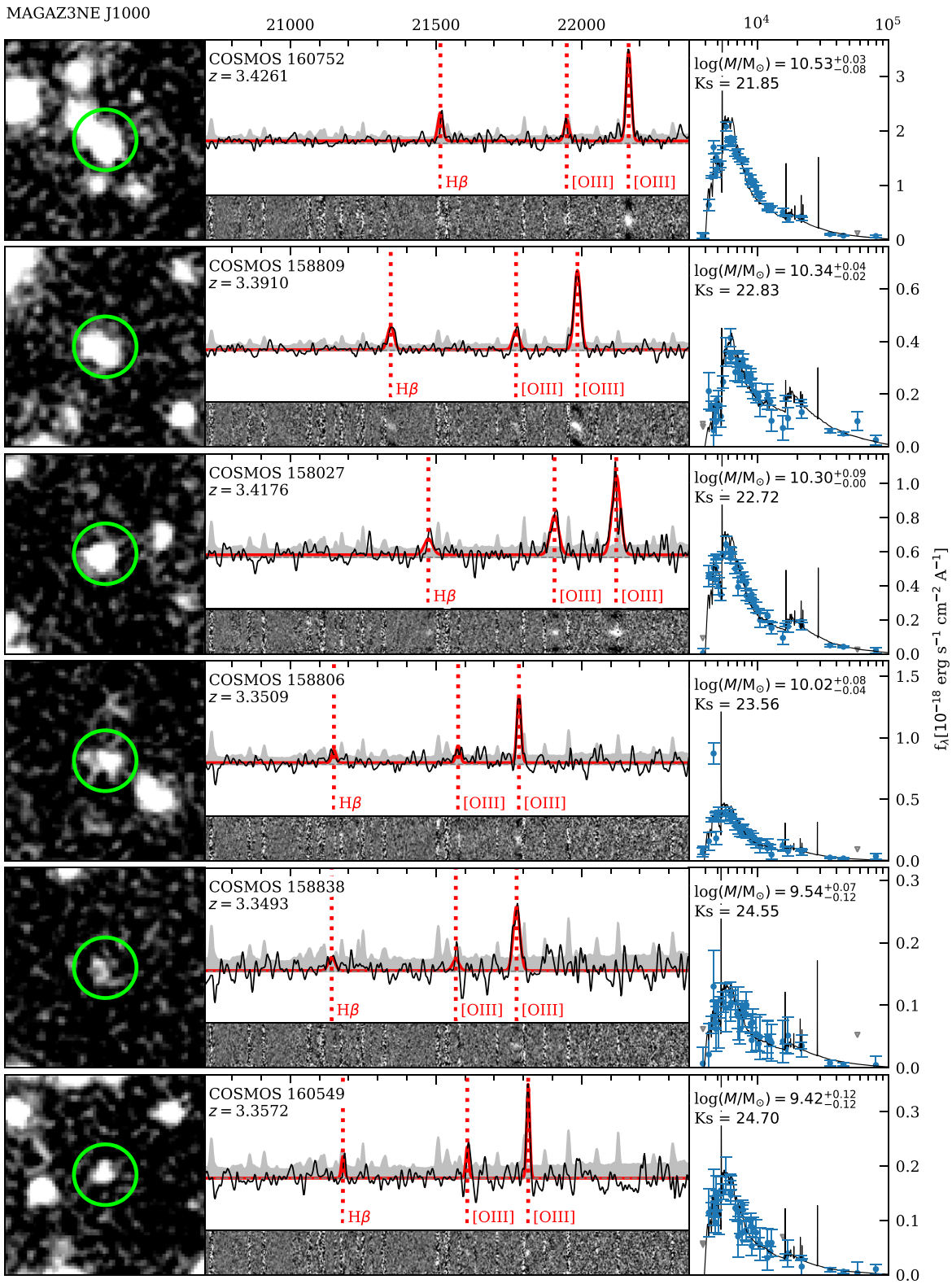

Figure 6. (Continued.)

strongly dependent on stellar mass. Van der Burg et al. (van der Burg et al. 2020) concluded that a substantially different quenching mode must operate in dense environments at early times.

Van der Burg et al. (van der Burg et al. 2020) explored various toy models to interpret their observations showing that they could be reproduced either if the cluster members (i) quenched through the same processes as those in the field but simply did so at an earlier time, a scenario they dubbed "early mass quenching," or (ii) underwent a form of environmental quenching that was mass dependent and, therefore, was significantly different from mass-independent environmental

quenching that has been suggested to occur in the local universe.

We do not yet know the cause of the quenching observed in MAGAZ3NE J0959 but it is intriguing to note that it does appear to be mass dependent, which is analogous to the results presented in van der Burg et al. (2020). Studies of $1 < z < 1.5$ clusters have determined the environmental quenching timescale, t_Q, for their members to be about 1 Gyr, meaning that "classical" quenching would be expected to begin at $z \sim 2$ (e.g., Muzzin et al. 2014; Foltz et al. 2018). While it is certainly possible that environmental processes might be responsible for the quenching observed in MAGAZ3NE J0959 (scenario "i" suggested by van der Burg et al.) it seems almost certain that those environmental processes would be different from the processes responsible for "classical" quenching in the low-redshift universe. Equally possible is that we might be witnessing "early mass quenching" (scenario "ii" suggested by van der Burg et al.). The fact that we observe a high quenched fraction of galaxies in MAGAZ3NE J0959 (Section 4.2) provides additional evidence in support of an "early mass quenching" or "accelerated evolution" interpretation but additional systems will be required in order to gain further insight.

5.2. BCG Formation and the Importance of Self versus Environmental Regulation

The stellar mass of UMG 179370 (MAGAZ3NE J0959) is $M_\star = 2.34^{+0.23}_{-0.34} \times 10^{11}\,M_\odot$, and the stellar mass of UMG 160748 (MAGAZ3NE J1000) is $M_\star = 2.95^{+0.21}_{-0.20} \times 10^{11}\,M_\odot$. Based on stellar mass, and utilizing the stellar mass–halo mass relation, at $z \sim 3$ each of these UMGs would be expected to reside in a halo of total mass equal to about $10^{13}\,M_\odot$ (Martizzi et al. 2012; Behroozi et al. 2013, 2019). It is, therefore, very likely that these two UMGs are the progenitors of Brightest Cluster Galaxies (BCGs) seen in virialized massive clusters at lower redshift (De Lucia & Blaizot 2007; Von Der Linden et al. 2007; Bernardi 2009; Pipino et al. 2011; Loubser et al. 2018; Ragone-Figueroa et al. 2018).

Simulations predict that the majority of stars that end up in present-day BCGs form at $z > 4$, but that the majority of the present-day stellar mass does not assemble until $z < 1.5$, meaning that a BCG would typically be expected to grow by a factor of about 5–10 between $z = 3$ and $z = 0$ (De Lucia & Blaizot 2007; Martizzi et al. 2012; Contini et al. 2018; Ragone-Figueroa et al. 2018; Henden et al. 2020). Our observations are consistent with this scenario whereby BCGs form most of their stars early, i.e., have old stellar ages locally (Thomas et al. 2005; Smith et al. 2012; McDermid et al. 2015; Citro et al. 2016; Webb et al. 2020), with most assembly at late times occurring via mergers/accretion (Lidman et al. 2012, 2013; Oliva-Altamirano et al. 2014; Webb et al. 2015; Delahaye et al. 2017). While the exact evolutionary path of UMG 179370 or UMG 160748 cannot be determined from these observations, they are likely destined to evolve to have stellar masses of $M_\star \gtrsim 10^{12}\,M_\odot$ and be found in Coma-mass (or greater) type halos by the present day.

This raises another fascinating question: the importance of self-regulation versus environmental regulation (e.g., Muzzin et al. 2012). Both UMGs have undergone recent, rapid star formation quenching (Forrest et al. 2020b), but we are currently unable to determine whether it was the environment itself that was the cause of the quenching, or whether they underwent "early mass quenching" because they happened to lie in an overdense environment (Section 4.2).

Further analysis will be required to determine whether UMGs are found preferentially in high-density environments or whether UMG 179370, which happens to be the oldest UMG in the sample (Forrest et al. 2020b), is an outlier. Our ongoing MAGAZ3NE survey should yield more information on the environments of these intriguing systems.

5.3. The Extended Forming Protocluster MAGAZ3NE J0959/J1000

Protoclusters MAGAZ3NE J0959 and MAGAZ3NE J1000 are separated by 17.85′ that corresponds to a comoving separation of 34.7 Mpc or a physical separation of 7.95 Mpc at $z = 3.37$. This separation is consistent with numerical simulations that follow the early stages of galaxy formation within forming protoclusters over similar scales (Angulo et al. 2012; Chiang et al. 2013; Muldrew et al. 2015). Based on predictions of the size of protoclusters at this epoch, it is quite possible that the MAGAZ3NE J0959/J1000 system will evolve into a "Coma"-type (or even more massive) cluster by the present day. However, because we lack information about the tangential velocities of the members of the extended protocluster MAGAZ3NE J0959/J1000 system, we cannot conclude this unequivocally. We can only conclude that we are either witnessing the seeds of a low-redshift massive cluster (if the protoclusters merge) or a supercluster system (if they do not).

6. Conclusions

In this paper we presented the discovery of two new protoclusters, MAGAZ3NE J0959 (38 members) at $z = 3.37$, and MAGAZ3NE J1000 (20 members) at $z = 3.38$. In contrast to commonly used techniques that have previously been utilized to identify protoclusters, these new systems were discovered using a different approach. They were identified neither by targeting LBG, LAE, HAE, or DSFG overdensities, nor by targeting commonly utilized "signposts" such as HZRG, QSO, or DSFGs. Rather, protoclusters MAGAZ3NE J0959 and MAGAZ3NE J1000 were identified as photometric overdensities around spectroscopically confirmed UMGs in the course of carrying out the MAGAZ3NE survey of UMGs and their environments at $3 < z < 4$. While UMGs may also be thought of as signposts, it remains to be seen whether they commonly exist in overdense environments and, therefore, whether or not they will prove useful as signposts to identify high-redshift protoclusters.

Notably, and in marked contrast to protoclusters previously reported at this epoch that have been found to predominantly contain star-forming members, MAGAZ3NE J0959 was found to have an elevated fraction of quiescent galaxies relative to the coeval field. This high quenched fraction provides a striking and important counterexample to the previously reported pervasiveness of star-forming galaxies in protoclusters at $z > 2$ and suggests, instead, that protoclusters exist in a diversity of evolutionary states in the early universe.

We do not yet know the cause of the quenching observed in MAGAZ3NE J0959 but, intriguingly, it appears to be mass dependent (increasing with increasing stellar mass). This is in stark contrast to mass-independent "classical" environmental quenching observed in the local universe, but in agreement with recent results at $1 < z < 1.5$ from the GOGREEN survey.

Whether we are witnessing "early mass quenching" or nontraditional "environmental quenching" will require larger samples to determine.

Both UMGs have undergone recent, rapid star formation quenching (Forrest et al. 2020b), but we are currently unable to determine whether it was the environment itself that was the cause of the quenching, or whether they underwent "early mass quenching" because they happened to lie in an overdense environment. Determining the relative importance of self-regulation versus environmental regulation will also require larger samples.

Based on their stellar mass and the stellar mass–halo mass relation, we concluded that UMG 179370 and UMG 160748 reside in halos of $\sim 10^{13}\,M_{\odot}$ at $z \sim 3$. They may well be the descendants of the population of highly dust-obscured massive star-forming galaxies discovered at $z > 5$ (see Forrest et al. 2020b, 2020a for more discussion). It is also highly likely that UMG 179370 and UMG 160748 are the progenitors of BCGs seen in virialized massive clusters at lower redshift. While the exact evolutionary paths of UMG 179370 and UMG 160748 cannot be predicted, the observations presented here show that very massive galaxies can form and quench surprisingly early during protocluster formation.

Protoclusters MAGAZ3NE J0959 and MAGAZ3NE J1000 are separated by 35 comoving Mpc, in good agreement with predictions from simulations regarding the size of "Coma"-type cluster progenitors forming at this epoch. Irrespective of whether or not MAGAZ3NE J0959 and MAGAZ3NE J1000 will actually merge by $z = 0$, we are undoubtedly witnessing the seeds of a low-redshift supercluster system.

The MAGAZ3NE J0959/J1000 protocluster system presented here was discovered in a field totaling only about 0.84 deg^2 in area. Future ground and space telescopes with the capability to survey significantly wider areas, e.g., the James Webb Space Telescope (Gardner et al. 2006), the Vera C. Rubin Observatory (LSST Science Collaboration et al. 2009), the Euclid Space Telescope (Laureijs et al. 2011), and the Nancy Grace Roman Space Telescope (Spergel et al. 2015) will undoubtedly facilitate the discovery of larger samples, allowing better insight into the uniqueness of MAGAZ3NE J0959, and helping to propel our understanding of the formation of UMGs and protoclusters into the even earlier universe.

This work was supported by the National Science Foundation through grant Nos. AST-1513473, AST-1517863, AST-1518257, and AST-1815475, by HST program number GO-15294, by UNAB internal grant DI-12-19/R, and by grant Nos. 80NSSC17K0019 and NNX16AN49G issued through the NASA Astrophysics Data Analysis Program (ADAP). Support for program number GO-15294 was provided by NASA through a grant from the Space Telescope Science Institute, which is operated by the Association of Universities for Research in Astronomy, Incorporated, under NASA contract NAS5-26555.

The data presented herein were obtained at the W. M. Keck Observatory, which is operated as a scientific partnership among the California Institute of Technology, the University of California, and the National Aeronautics and Space Administration. The Observatory was made possible by the generous financial support of the W. M. Keck Foundation. The authors wish to recognize and acknowledge the very significant cultural role and reverence that the summit of Maunakea has always had within the indigenous Hawaiian community. We are most fortunate to have the opportunity to conduct observations from this mountain.

ORCID iDs

Ian McConachie https://orcid.org/0000-0002-2446-8770
Gillian Wilson https://orcid.org/0000-0002-6572-7089
Ben Forrest https://orcid.org/0000-0001-6003-0541
Z. Cemile Marsan https://orcid.org/0000-0002-7248-1566
Adam Muzzin https://orcid.org/0000-0002-9330-9108
M. C. Cooper https://orcid.org/0000-0003-1371-6019
Marianna Annunziatella https://orcid.org/0000-0002-8053-8040
Danilo Marchesini https://orcid.org/0000-0001-9002-3502
Jeffrey C. C. Chan https://orcid.org/0000-0001-6251-3125
Percy Gomez https://orcid.org/0000-0003-0408-9850
Mohamed H. Abdullah https://orcid.org/0000-0003-3595-7147
Paolo Saracco https://orcid.org/0000-0003-3959-2595

References

Abdullah, M. H., Wilson, G., Klypin, A., et al. 2020, ApJS, 246, 2
Adams, S. M., Martini, P., Croxall, K. V., Overzier, R. A., & Silverman, J. D. 2015, MNRAS, 448, 1335
Aihara, H., Armstrong, R., Bickerton, S., et al. 2018, PASJ, 70, S8
Angulo, R. E., Springel, V., White, S. D. M., et al. 2012, MNRAS, 426, 2046
Ashby, M. L. N., Caputi, K. I., Cowley, W., et al. 2018, ApJS, 237, 39
Balogh, M. L., McGee, S. L., Mok, A., et al. 2016, MNRAS, 456, 4364
Beers, T. C., Flynn, K., & Gebhardt, K. 1990, AJ, 100, 32
Behroozi, P., Wechsler, R. H., Hearin, A. P., & Conroy, C. 2019, MNRAS, 488, 3143
Behroozi, P. S., Wechsler, R. H., & Conroy, C. 2013, ApJ, 770, 57
Belli, S., Newman, A. B., & Ellis, R. S. 2019, ApJ, 874, 17
Bernardi, M. 2009, MNRAS, 395, 1491
Binggeli, B., Tammann, G. A., & Sandage, A. 1987, AJ, 94, 251
Brammer, G. B., van Dokkum, P. G., & Coppi, P. 2008, ApJ, 686, 1503
Bruzual, G., & Charlot, S. 2003, MNRAS, 344, 1000
Calzetti, D., Armus, L., Bohlin, R. C., et al. 2000, ApJ, 533, 682
Capak, P., Abraham, R. G., Ellis, R. S., et al. 2007, ApJS, 172, 284
Capak, P. L., Riechers, D., Scoville, N. Z., et al. 2011, Natur, 470, 233
Casey, C. M. 2016, ApJ, 824, 36
Casey, C. M., Cooray, A., Capak, P., et al. 2015, ApJL, 808, L33
Chabrier, G. 2003, PASP, 115, 763
Champagne, J. B., Casey, C. M., Zavala, J. A., et al. 2021, ApJ, 913, 110
Chapman, S. C., Blain, A., Ibata, R., et al. 2009, ApJ, 691, 560
Cheng, T., Clements, D. L., Greenslade, J., et al. 2019, MNRAS, 490, 3840
Chiang, Y.-K., Overzier, R., & Gebhardt, K. 2013, ApJ, 779, 127
Chiang, Y.-K., Overzier, R., & Gebhardt, K. 2014, ApJL, 782, L3
Chiang, Y.-K., Overzier, R. A., Gebhardt, K., & Henriques, B. 2017, ApJL, 844, L23
Chiang, Y.-K., Overzier, R. A., Gebhardt, K., et al. 2015, ApJ, 808, 37
Citro, A., Pozzetti, L., Moresco, M., & Cimatti, A. 2016, A&A, 592, A19
Clements, D. L., Braglia, F. G., Hyde, A. K., et al. 2014, MNRAS, 439, 1193
Contini, E., Yi, S. K., & Kang, X. 2018, MNRAS, 479, 932
Cooke, E. A., Hatch, N. A., Stern, D., et al. 2016, ApJ, 816, 83
Cooper, M. C., Coil, A. L., Gerke, B. F., et al. 2010, MNRAS, 409, 337
Cooper, M. C., Newman, J. A., Coil, A. L., et al. 2007, MNRAS, 376, 1445
Cooper, M. C., Newman, J. A., Croton, D. J., et al. 2006, MNRAS, 370, 198
Cucciati, O., Lemaux, B. C., Zamorani, G., et al. 2018, A&A, 619, A49
Cucciati, O., Zamorani, G., Lemaux, B. C., et al. 2014, A&A, 570, A16
Daddi, E., Jin, S., Strazzullo, V., et al. 2017, ApJL, 846, L31
Dannerbauer, H., Kurk, J. D., De Breuck, C., et al. 2014, A&A, 570, A55
Darvish, B., Mobasher, B., Sobral, D., et al. 2016, ApJ, 825, 113
Darvish, B., Scoville, N. Z., Martin, C., et al. 2020, ApJ, 892, 8
De Lucia, G., & Blaizot, J. 2007, MNRAS, 375, 2
Delahaye, A. G., Webb, T. M. A., Nantais, J., et al. 2017, ApJ, 843, 126
Dey, A., Lee, K.-S., Reddy, N., et al. 2016, ApJ, 823, 11
Diener, C., Lilly, S. J., Knobel, C., et al. 2013, ApJ, 765, 109
Diener, C., Lilly, S. J., Ledoux, C., et al. 2015, ApJ, 802, 31
Dressler, A. 1980, ApJ, 236, 351
Fabian, A. C. 2012, ARA&A, 50, 455
Farouki, R., & Shapiro, S. L. 1981, ApJ, 243, 32
Fasano, G., Poggianti, B. M., Bettoni, D., et al. 2015, MNRAS, 449, 3927

Fasano, G., Vanzella, E., Dressler, A., et al. 2012, MNRAS, 420, 926
Finoguenov, A., Guzzo, L., Hasinger, G., et al. 2007, ApJS, 172, 182
Foltz, R., Wilson, G., Muzzin, A., et al. 2018, ApJ, 866, 136
Forrest, B., Annunziatella, M., Wilson, G., et al. 2020a, ApJL, 890, L1
Forrest, B., Marsan, Z. C., Annunziatella, M., et al. 2020b, ApJ, 903, 47
Forrest, B., Tran, K.-V. H., Broussard, A., et al. 2017, ApJL, 838, L12
Galametz, A., Stern, D., De Breuck, C., et al. 2012, ApJ, 749, 169
Gardner, J. P., Mather, J. C., Clampin, M., et al. 2006, SSRv, 123, 485
Geach, J. E., Sobral, D., Hickox, R. C., et al. 2012, MNRAS, 426, 679
Gehrels, N. 1986, ApJ, 303, 336
Gómez, P. L., Nichol, R. C., Miller, C. J., et al. 2003, ApJ, 584, 210
Goto, T., Yamauchi, C., Fujita, Y., et al. 2003, MNRAS, 346, 601
Greenslade, J., Clements, D. L., Cheng, T., et al. 2018, MNRAS, 476, 3336
Guaita, L., Pompei, E., Castellano, M., et al. 2020, A&A, 640, A107
Gunn, J. E., Gott, J., & Richard, I. 1972, ApJ, 176, 1
Harikane, Y., Ouchi, M., Ono, Y., et al. 2019, ApJ, 883, 142
Hatch, N. A., De Breuck, C., Galametz, A., et al. 2011, MNRAS, 410, 1537
Henden, N. A., Puchwein, E., & Sijacki, D. 2020, MNRAS, 498, 2114
Hildebrandt, H., Pielorz, J., Erben, T., et al. 2009, A&A, 498, 725
Hopkins, P. F., Kereš, D., Oñorbe, J., et al. 2014, MNRAS, 445, 581
Horne, K. 1986, PASP, 98, 609
Hung, C.-L., Casey, C. M., Chiang, Y.-K., et al. 2016, ApJ, 826, 130
Ivison, R., Smail, I., Dunlop, J., & Jenner, C. 2001, in Deep Millimeter Surveys: Implications for Galaxy Formation and Evolution, ed. J. D. Lowenthal & D. H. Hughes (Singapore: World Scientific), 135
Jian, H.-Y., Lin, L., Lin, K.-Y., et al. 2017, ApJ, 845, 74
Jian, H.-Y., Lin, L., Oguri, M., et al. 2018, PASJ, 70, S23
Kauffmann, G., White, S. D. M., Heckman, T. M., et al. 2004, MNRAS, 353, 713
Kawinwanichakij, L., Papovich, C., Quadri, R. F., et al. 2017, ApJ, 847, 134
Koyama, Y., Polletta, M. d. C., Tanaka, I., et al. 2020, MNRAS, 503, L1
Kriek, M., van Dokkum, P. G., Labbé, I., et al. 2009, ApJ, 700, 221
Kubo, M., Umehata, H., Matsuda, Y., et al. 2021, ApJ, 919, 6
Larson, R. B., Tinsley, B. M., & Caldwell, C. N. 1980, ApJ, 237, 692
Laureijs, R., Amiaux, J., Arduini, S., et al. 2011, arXiv:1110.3193
Lee, K.-G., Hennawi, J. F., White, M., Croft, R. A. C., & Ozbek, M. 2014, ApJ, 788, 49
Lee, K.-G., Hennawi, J. F., White, M., et al. 2016, ApJ, 817, 160
Lee-Brown, D. B., Rudnick, G. H., Momcheva, I. G., et al. 2017, ApJ, 844, 43
Lemaux, B. C., Cucciati, O., Tasca, L. A. M., et al. 2014, A&A, 572, A41
Lemaux, B. C., Le Fèvre, O., Cucciati, O., et al. 2018, A&A, 615, A77
Lemaux, B. C., Lubin, L. M., Sawicki, M., et al. 2009, ApJ, 700, 20
Lemaux, B. C., Tomczak, A. R., Lubin, L. M., et al. 2019, MNRAS, 490, 1231
Li, P., Wang, H., Mo, H. J., Wang, E., & Hong, H. 2020, ApJ, 902, 75
Lidman, C., Iacobuta, G., Bauer, A. E., et al. 2013, MNRAS, 433, 825
Lidman, C., Suherli, J., Muzzin, A., et al. 2012, MNRAS, 427, 550
Lilly, S. J., Le Fèvre, O., Renzini, A., et al. 2007, ApJS, 172, 70
Long, A. S., Cooray, A., Ma, J., et al. 2020, ApJ, 898, 133
Loubser, S. I., Hoekstra, H., Babul, A., & O'Sullivan, E. 2018, MNRAS, 477, 335
LSST Science Collaboration, Abell, P. A., Allison, J., et al. 2009, arXiv:0912.0201
Marchesini, D., Whitaker, K. E., Brammer, G., et al. 2010, ApJ, 725, 1277
Marsan, Z. C., Marchesini, D., Brammer, G. B., et al. 2015, ApJ, 801, 133
Marsan, Z. C., Marchesini, D., Brammer, G. B., et al. 2017, ApJ, 842, 21
Marsan, Z. C., Muzzin, A., Marchesini, D., et al. 2022, ApJ, 924, 25
Martis, N. S., Marchesini, D., Brammer, G. B., et al. 2016, ApJL, 827, L25
Martizzi, D., Teyssier, R., & Moore, B. 2012, MNRAS, 420, 2859
McCracken, H. J., Milvang-Jensen, B., Dunlop, J., et al. 2012, A&A, 544, A156
McDermid, R. M., Alatalo, K., Blitz, L., et al. 2015, MNRAS, 448, 3484
McLean, I. S., Steidel, C. C., Epps, H., et al. 2010, Proc. SPIE, 7735, 77351E
McLean, I. S., Steidel, C. C., Epps, H. W., et al. 2012, Proc. SPIE, 8446, 84460J
Merlin, E., Fontana, A., Castellano, M., et al. 2018, MNRAS, 473, 2098
Miley, G., & De Breuck, C. 2008, A&ARv, 15, 67
Miller, T. B., Chapman, S. C., Aravena, M., et al. 2018, Natur, 556, 469
Moore, B., Katz, N., Lake, G., Dressler, A., & Oemler, A. 1996, Natur, 379, 613
Muldrew, S. I., Hatch, N. A., & Cooke, E. A. 2015, MNRAS, 452, 2528
Muzzin, A., Marchesini, D., Stefanon, M., et al. 2013, ApJS, 206, 8
Muzzin, A., van der Burg, R. F. J., McGee, S. L., et al. 2014, ApJ, 796, 65
Muzzin, A., Wilson, G., Yee, H. K. C., et al. 2012, ApJ, 746, 188
Nantais, J. B., Muzzin, A., van der Burg, R. F. J., et al. 2017, MNRAS, 465, L104
Nantais, J. B., van der Burg, R. F. J., Lidman, C., et al. 2016, A&A, 592, A161
Newman, A. B., Ellis, R. S., Andreon, S., et al. 2014, ApJ, 788, 51
Oemler, A. J. 1974, ApJ, 194, 1
Oke, J. B., & Gunn, J. E. 1983, ApJ, 266, 713
Oliva-Altamirano, P., Brough, S., Lidman, C., et al. 2014, MNRAS, 440, 762
Ouchi, M., Harikane, Y., Shibuya, T., et al. 2018, PASJ, 70, S13
Overzier, R. A. 2016, A&ARv, 24, 14
Pavesi, R., Riechers, D. A., Sharon, C. E., et al. 2018, ApJ, 861, 43
Peng, Y.-j., Lilly, S. J., Kovač, K., et al. 2010, ApJ, 721, 193
Pentericci, L., Roettgering, H. J. A., Miley, G. K., Carilli, C. L., & McCarthy, P. 1997, A&A, 326, 580
Pintos-Castro, I., Yee, H. K. C., Muzzin, A., Old, L., & Wilson, G. 2019, ApJ, 876, 40
Pipino, A., Szabo, T., Pierpaoli, E., MacKenzie, S. M., & Dong, F. 2011, MNRAS, 417, 2817
Planck Collaboration, Ade, P. A. R., Aghanim, N., et al. 2016, A&A, 596, A100
Planck Collaboration, Aghanim, N., Altieri, B., et al. 2015, A&A, 582, A30
Quadri, R. F., Williams, R. J., Franx, M., & Hildebrandt, H. 2012, ApJ, 744, 88
Ragone-Figueroa, C., Granato, G. L., Ferraro, M. E., et al. 2018, MNRAS, 479, 1125
Roberts, I. D., & Parker, L. C. 2019, MNRAS, 490, 773
Sanders, D. B., Salvato, M., Aussel, H., et al. 2007, ApJS, 172, 86
Saracco, P., Marchesini, D., La Barbera, F., et al. 2020, ApJ, 905, 40
Shapley, A. E., Steidel, C. C., Erb, D. K., et al. 2005, ApJ, 626, 698
Shi, K., Lee, K.-S., Dey, A., et al. 2019, ApJ, 871, 83
Shi, K., Toshikawa, J., Lee, K. S., et al. 2021, ApJ, 911, 46
Smith, R. J., Lucey, J. R., Price, J., Hudson, M. J., & Phillipps, S. 2012, MNRAS, 419, 3167
Spergel, D., Gehrels, N., Baltay, C., et al. 2015, arXiv:1503.03757
Spitler, L. R., Labbé, I., Glazebrook, K., et al. 2012, ApJL, 748, L21
Springel, V., White, S. D. M., Jenkins, A., et al. 2005, Natur, 435, 629
Steidel, C. C., Adelberger, K. L., Dickinson, M., et al. 1998, ApJ, 492, 428
Steidel, C. C., Adelberger, K. L., Shapley, A. E., et al. 2005, ApJ, 626, 44
Strazzullo, V., Pannella, M., Mohr, J. J., et al. 2019, A&A, 622, A117
Thomas, D., Maraston, C., Bender, R., & Mendes de Oliveira, C. 2005, ApJ, 621, 673
Toshikawa, J., Uchiyama, H., Kashikawa, N., et al. 2018, PASJ, 70, S12
Tran, K.-V. H., Alcorn, L. Y., Kacprzak, G. G., et al. 2017, ApJ, 834, 101
van der Burg, R. F. J., Rudnick, G., Balogh, M. L., et al. 2020, A&A, 638, A112
van der Wel, A., Noeske, K., Bezanson, R., et al. 2016, ApJS, 223, 29
Von Der Linden, A., Best, P. N., Kauffmann, G., & White, S. D. M. 2007, MNRAS, 379, 867
Wang, H., Mo, H. J., Chen, S., et al. 2018, ApJ, 852, 31
Wang, T., Elbaz, D., Daddi, E., et al. 2016, ApJ, 828, 56
Webb, K., Balogh, M. L., Leja, J., et al. 2020, MNRAS, 498, 5317
Webb, T. M. A., Muzzin, A., Noble, A., et al. 2015, ApJ, 814, 96
Wetzel, A. R., Tinker, J. L., & Conroy, C. 2012, MNRAS, 424, 232
Whitaker, K. E., Labbé, I., van Dokkum, P. G., et al. 2011, ApJ, 735, 86
Williams, R. J., Quadri, R. F., Franx, M., van Dokkum, P., & Labbé, I. 2009, ApJ, 691, 1879
Wuyts, S., Labbé, I., Franx, M., et al. 2007, ApJ, 655, 51
Yuan, T., Nanayakkara, T., Kacprzak, G. G., et al. 2014, ApJL, 795, L20
Zavala, J. A., Casey, C. M., Scoville, N., et al. 2019, ApJ, 887, 183